

Integrating One-Shot View Planning with a Single Next-Best View via Long-Tail Multiview Sampling

Sicong Pan, Hao Hu, Hui Wei, Nils Dengler, Tobias Zaenker, Murad Dawood and Maren Bennewitz

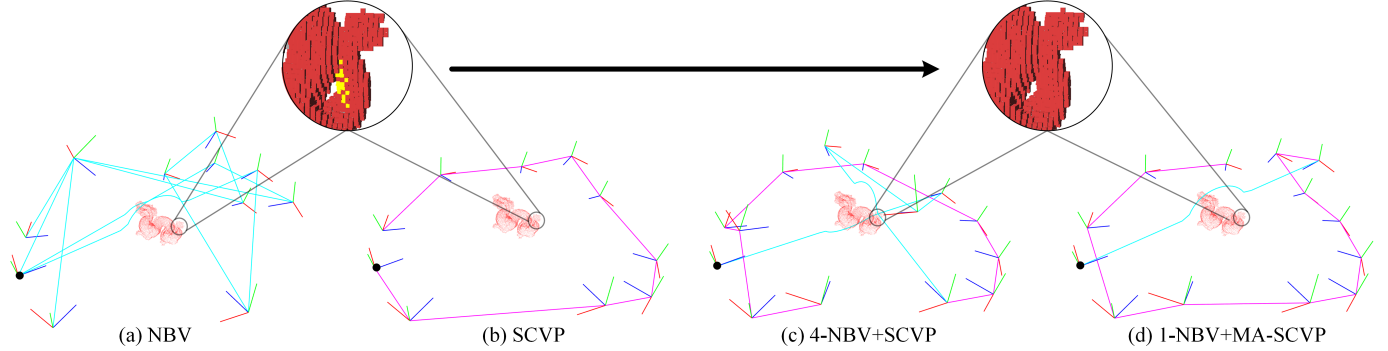


Fig. 1: Comparative results of reconstructing an unknown object: Each method is depicted through reconstructed 3D models (red point clouds), local paths (cyan), global paths (purple), views (red-green-blue coordinate systems), and the same initial view (black circle). In (a) and (b), it is observed that both the iterative NBV method and the one-shot set-covering view-planning (SCVP) network fail to provide complete surface details (yellow voxels in enlarged areas). To address these missing surfaces, we introduce a novel combined pipeline that incorporates four NBVs before activating the SCVP network, as shown in (c). However, this approach requires more NBVs and paths (4 NBVs with 4 long local paths). Therefore, we propose the multiview-activated MA-SCVP network, trained on our innovative long-tail multiview dataset as shown in (d), to enhance the reconstruction efficiency (requiring 1 NBV with 1 local path) while maintaining high-quality reconstruction.

Abstract—Existing view planning systems either adopt an iterative paradigm using next-best views (NBV) or a one-shot pipeline relying on the set-covering view-planning (SCVP) network. However, neither of these methods can concurrently guarantee both high-quality and high-efficiency reconstruction of 3D unknown objects. To tackle this challenge, we introduce a crucial hypothesis: with the availability of more information about the unknown object, the prediction quality of the SCVP network improves. There are two ways to provide extra information: (1) leveraging perception data obtained from NBVs, and (2) training on an expanded dataset of multiview inputs. In this work, we introduce a novel combined pipeline that incorporates a single NBV before activating the proposed multiview-activated (MA-)SCVP network. The MA-SCVP is trained on a multiview dataset generated by our long-tail sampling method, which addresses the issue of unbalanced multiview inputs and enhances the network performance. Extensive simulated experiments substantiate that our system demonstrates a significant surface coverage increase and a substantial 45% reduction in movement cost compared to state-of-the-art systems. Real-world experiments justify the capability of our system for generalization and deployment.

Index Terms—Object reconstruction, Active vision, View planning, Set covering optimization, Long tail distribution

This work was supported by the NSFC Project under Grant 61771146 (Corresponding author: Hui Wei).

Sicong Pan, Hao Hu, and Hui Wei are with the Laboratory of Algorithms for Cognitive Models, School of Computer Science, Fudan University, China (email: span@uni-bonn.de, hao.hu@intel.com, weihui@fudan.edu.cn).

Sicong Pan, Nils Dengler, Tobias Zaenker, Murad Dawood, and Maren Bennewitz are with the Humanoid Robots Lab, Computer Science Institute VI, University of Bonn, Germany (email: span@uni-bonn.de, dengler@cs.uni-bonn.de, tzaenker@cs.uni-bonn.de, dawood@cs.uni-bonn.de, maren@cs.uni-bonn.de).

Hao Hu is with Intel Asia-Pacific Research & Development Ltd.

I. INTRODUCTION

A complete 3D model of an object is important for various autonomous tasks, such as crop monitoring in the agriculture domain [1], pushing manipulation in confined spaces [2], and grasping in tabletop scenarios [3]. Facing an unknown environment, active vision systems based on view planning [4] are widely studied due to their ability to automatically reconstruct a *prior unknown* object. In this work, we address the view planning challenge in robotic active vision, specifically tailored for achieving both high-quality and high-efficiency 3D reconstruction of unknown objects in tabletop scenarios.

Existing view planning systems fall into either an *iterative* paradigm utilizing the next-best-view (NBV) evaluation [5] or a *one-shot* pipeline relying on the set-covering view-planning (SCVP) network [6]. In the iterative paradigm, the robot uses stochastic state analysis [7] or pre-learned knowledge [8] to plan an NBV after each sensor scan, navigates to that NBV, and repeats this process until a specific stop criterion is met. However, this iterative paradigm lacks global path planning capabilities as shown in Fig. 1(a). Specifically, the robot can only plan a long local path to the NBV [8] in each iteration. To improve the reconstruction efficiency, we have previously suggested one-shot view planning [6], that utilizes SCVP to predict a set of views and compute a global path only once as shown in Fig. 1(b). By accessing all required views at once, the robot performs much faster than iterative systems.

However, neither the iterative nor the one-shot method guarantees a high-quality reconstruction. As shown in the enlarged area in Fig. 1(a) and (b), the 3D models reconstructed by these methods lack surface details that may be crucial features for subsequent tasks, such as grasping and watertight meshing. The insufficiency in surface details within iterative methods

primarily arises from the hand-crafted heuristic stop criterion, which determines the required number of views. Due to the resolution constraints, these methods tend to stop prematurely with an insufficient number of views. In contrast, the one-shot SCVP method introduces a built-in auto-stop criterion learned from set covering, which is to find the smallest set of views for full surface coverage. Although SCVP does take into account the stop criterion, the insufficiency in surface details is attributed to its dependence on a singleview input, which provides inadequate information about the object to be reconstructed in an unknown environment.

In the unknown environment, one obvious hypothesis is that the more information you have, the more accurate your predictions will be. Based on this insight, we assume that with the availability of more information about the object to be reconstructed, the prediction quality of the SCVP network improves. In this work, we explore two distinct solutions to provide extra information to SCVP: (1) *online* leveraging more perception data obtained from NBVs as SCVP input, and (2) *offline* training on an expanded dataset of multiview inputs. For the first solution, we propose a combined auto-stop pipeline that selects a few NBVs before activating the SCVP network. As shown in Fig. 1(c), this pipeline does increase the surface coverage, but extra NBVs and paths, especially four long NBV paths, are required to finish the reconstruction.

To further improve efficiency while maintaining high-quality reconstruction, we adopt the second solution because multiview inputs contain more surface information. Different from singleview inputs, multiview inputs show an imbalance in importance to network training. We observe a vital phenomenon in terms of the gain of surface coverage: the first 1-3 views cover approximately 80% of the surface, whereas subsequent views contribute only to the remaining 20%, resembling a classic long-tail distribution [9]. Consequently, multiview inputs containing perception data from fewer views should be deemed more important. For instance, a 15-view input case may already cover 97% surfaces, making it less valuable for training. Therefore, we devise a long-tail sampling strategy to align the number of views in multiview inputs with the long-tail distribution of surface coverage gain. Moreover, we suggest a multiview-activated (MA)-SCVP network architecture, which adds a view state as input, to enhance training on the long-tail multiview dataset. The advantages of employing the long-tail dataset and the MA-SCVP network architecture are validated through experimental studies on network training.

In simulated reconstruction tests, the MA-SCVP network trained on our long-tail dataset exhibits superior overall performance compared to traditional sampling methods [8], [10]. Notably, training on our long-tail dataset also improves the surface coverage of the first few NBVs obtained from NBV networks. This enhancement facilitates a more seamless integration of the MA-SCVP with NBV networks. Ablation studies conducted on our combined pipeline reveal that, with the assistance of training on our long-tail multiview dataset, only a single NBV is required to provide additional information before activating the MA-SCVP network. Fig. 1(d) illustrates an example of the integration of one-shot view planning with a single NBV through our long-tail multiview

sampling, reducing the required NBVs and paths.

Extensive simulated experiments provide compelling evidence that our system outperforms both iterative baselines (including the heuristic stop criterion) and the one-shot baseline, yielding a significant increase in surface coverage and a substantial 45% reduction in movement cost. Subsequently, since the object center and size are not known in advance in a real-world environment, we assess our system using the dynamic object bounding box to justify its generalization capability. In real-world comparative tests, our system consistently validates the claims established in our simulations. Finally, we analyze how our system of providing extra information enhances the reconstruction quality in terms of object test case complexity.

The contributions of this work are summarized as follows:

- Unlike singleview inputs in the SCVP network, we propose a long-tail sampling method to generate a multiview dataset, offering extra information during the training phase. This long-tail sampling addresses unbalanced importance among multiview inputs, presenting an efficient training dataset compared to traditional sampling.
- Unlike the heuristic stop criterion commonly employed in NBV methods, our system includes an auto-stop criterion learned from set covering. We propose the MA-SCVP network architecture to train on our long-tail multiview dataset, ensuring a sufficient number of predicted views (stop criterion) for a high-quality reconstruction.
- We propose a novel combined pipeline that incorporates a few NBVs before embarking on one-shot view planning. Ablation studies confirm that a single NBV is adequate for providing extra information during online data collection. Our system concurrently achieves both high-quality and high-efficiency unknown object reconstruction.
- We deploy our system on a robotic arm equipped with an RGB-D camera in a real-world environment. Comparative experiments demonstrate the robust generalization capabilities and reconstruction performance of our system.

To support reproducibility, our implementation is released at <https://github.com/psc0628/MA-SCVP>.

II. RELATED WORK

Active vision systems and view planning problems for 3D reconstruction, dating back to the 1980s [11], have been extensively studied [4], [12], [13] and continue to be a frontier area of robotic research [5], [14]. Depending on the moving area of robots, 3D reconstruction targets can be categorized as scenes or objects [5]. Scene reconstruction, also referred to as 3D exploration [15]–[17] requires mobile robots to *explore inside* a limited 3D volume and aims to reconstruct large structures. Since mobile robots experience cumulative errors and battery issues during long-distance travel, view planning focuses more on the path planning problems [18]. On the other hand, object reconstruction [19]–[21] requires robots to *observe outside* a limited 3D volume and aims to reconstruct a relatively small object with complex surface details. In this study, we concentrate on the reconstruction of small tabletop objects characterized by complex self-occluded surfaces that are an essential consideration for applications like industrial manufacturing [22] and agricultural plant reconstruction [23].

A. Next-Best-View Planning

Early research on view planning methods for object reconstruction used synthesis methods, whereby sensor views are directly chosen based on specific constraints represented by analytical functions [11], [24]. The synthesis method can be faster than the search-based method, but it lacks the capability to address occlusion issues, which is important for the modeling of complex surfaces.

Zeng *et al.* [5] summarized modern search-based view planning methods as a generate-and-test procedure. Since recently more learning-based methods emerged, we broaden this summary to the generalized generate-and-test procedure, as follows: (1) Generate a candidate view space (a number of candidate views) under some constraints or task requirements, such as the robot workspace and regions of interest [25]. (2) Test the candidate view space via a certain utility function to achieve the goal of view planning.

The fundamental differences between view planning methods lie in the definition of the utility function: goal (output), 3D representation (input), and optimization technique.

1) *Goal*: Active vision systems are typically designed for autonomous applications in unknown environments [4]. An iterative pipeline that selects an NBV maximizing the utility function for each sensor update is therefore commonly used. This makes sense due to the ability to monitor information gains in an unknown environment in real-time.

In addition, some works are based on multi-robot collaboration [26], [27], which assigns an NBV for each robot in an iteration by overlap awareness. Generally, in active vision, the goal of the utility function is defined as finding the NBV(s), and the view planning methods are also known as iterative NBV planning methods.

2) *3D Representation*: Active vision systems continuously collect detected information about an unknown environment to deal with uncertainties. The information is the representation of the 3D environment and the object. As an input to the utility function, it is clear that the choice of data structures strongly influences the view planning strategy [5].

Point cloud. Point cloud is the directly accessible data from sensor observations, such as (x,y,z) coordinates and color information of depth sensors [28]. It is straightforward to restore the surface details of an object [29].

Surface. Surface representation is the common form of 3D models [30] in computer graphics. The most popular discrete surface is the triangle mesh [31]. The continuous Poisson field can also be used for view planning [32]. The surface representation can capture fine details but more details have higher computational costs.

Voxel. Voxel representation is the discrete grid of the 3D space, usually stored in an octree or occupancy map [33]. Unlike point clouds and surfaces, voxels can describe unknown and empty spaces and are therefore the most commonly used in view planning [34]. Some related voxel representations, such as TSDF [35] and surfel [36], can be used to extract surfaces for better view planning. The principal disadvantage is its wastefulness of storage.

NeRF. Neural Radiance Field (NeRF) is an implicit representation of 3D space [37], stored in the network function by

taking a point on a ray direction as inputs and its color value with density as outputs. Researchers have increased interest in using NeRF for view planning [38]–[40] because it can reduce the storage costs of explicit representations.

3) *Optimization Technique*: There are two common optimization techniques to define the way to find NBV(s): search and learning. Another important difference is the additional constraints on the candidate view space.

Search. Search-based methods define heuristic functions on the 3D representations and select the best view of maximum utility. The candidate views have no other constraints and can be dynamic. Some of them are random or spherical sampled and can sample a large number while others are defined by heuristic functions and selected by certain requirements such as robot movement cost. Although the 3D representation varies, the heuristic functions have some common high-level features: frontier areas, boundary and shape analysis, and entropy and occlusion awareness.

For point cloud-based search, Border *et al.* [29] proposed density representation to define a frontier between fully and partially observed surfaces and later they [41], [42] handle occlusions to select NBVs that most improve an observation.

For surface-based search, Krigel *et al.* [43] purposed boundary and curve estimation of mesh for new surface information. Wu *et al.* [32] suggested gradient and smoothness confidence to quantify Poisson surfaces and Lee *et al.* [44] improved with primitive shape analysis to select NBVs.

For voxel-based search, Krainin *et al.* [45] modeled the information gain in terms of entropy and suggested the boundaries between occupied and unknown voxels. Vasquez-Gomez *et al.* [46], [47] proposed the area factor for perceiving unknown areas and handling overlap with previous scans. Daudelin and Campbell [48] proposed to use frontier voxels to model the object probability of belonging to the object surfaces. Delmerico *et al.* [7] summarized ray casting-based volumetric information gains and proposed rear side entropy, assuming that unknown areas behind the observed object surface are more likely to be the new object surface. Pan and Wei [49] proposed a max-flow-based global optimization for volumetric covering of predicted surfaces and later they [50] improved NBV selections by generalized maximum coverage.

For NeRF-based search, Lee *et al.* [51] proposed ray-based volumetric uncertainty and Sünderhauf *et al.* [52] proposed density-based ensemble uncertainty to select NBVs for better NeRF online learning.

Learning. Diverging from search-based methods, learning-based methods typically acquire the view-planning ability through end-to-end learning from the environment or data.

For reinforcement learning, these methods get the reward of the utility of a view directly from the environment and are usually trained in simulation. The candidate views are implicitly defined by states and actions. Peralta *et al.* [53] proposed the reward function of the percentage of observed surface points over the total number of surface points in the ground truth model. Zeng *et al.* [54] proposed the reward function of the coverage of the unknown area for fruit detection and mapping.

For deep learning, NBV planning is usually treated as classification problems, *i.e.*, an optimal view class is selected for

the current scene, which can be trained by a simulated dataset. The candidate views can be re-scaled with object size but they should be pre-defined, *e.g.*, on a sphere. With the development of voxel-based networks [55], Mendoza *et al.* [10] proposed NBVNet and later they analyzed the NBV regression [56]. Along with advances in networks of point cloud [57], Zeng *et al.* [8] proposed point-cloud-based PCNBV for scoring the views and Han *et al.* [58] proposed double-brunch-based DBNBV for ranking the views instead of scoring.

To sum up, in the field of NBV planning, search-based methods are the most developed and straightforward. However, facing the problem of time efficiency due to the potential large search space, a balance between accuracy and efficiency needs to be considered. Therefore, since learning-based methods do not require hand-crafted heuristics and can infer very fast after sufficient training, they are receiving more attention from current researchers. In this work, we also use deep learning techniques for fast inference.

B. One-Shot View Planning

Deep learning essentially learns prior knowledge from data and stores it in the network function. In particular, the NBV-based networks learn object local geometry and plan a view to locally maximize the coverage of the object surface [8], [10], [56], [58]. However, neural networks can be designed in a certain way to learn the global features of the object geometry. Wu *et al.* [26] proposed to use a point completion network to predict the shape of the plant and update a voxel grid to select the NBV. Monica and Aleotti [59] proposed a voxel-based network to predict the uncertainty of the environment (surface distribution of the object) and also plan NBV by voxel-based search. These methods confirm the ability of deep learning to learn global information.

However, these methods use deep learning to learn globally but plan views locally. Why not use networks to learn global information and directly predict a set of global views? This motivation brings us back to the goal of view planning. In addition to active vision systems, view planning is also used for inspection and reverse engineering tasks [60] where the environment and the object are known in advance, *e.g.*, given a prior 3D model. The goal is to find a view subset of the minimum size that simultaneously covers all object surfaces. Kaba *et al.* [61] formulate this model-based view planning as the set covering optimization problem (SCOP) and solve it through reinforcement learning. The variations of SCOP are further studied to improve the system performance in aerial modeling [62] and industrial manufacturing [63].

It seems promising to use deep learning to learn from model-based global view planning and also predict the smallest set of views covering all object surfaces. To achieve this goal, we have previously introduced the SCVP network [6] and the automatic supervised label generation by solving SCOP in simulation. We use a voxel-based network because it is easier to define the SCOP on structured surfaces (voxels) rather than unstructured surfaces (point clouds). Using deep learning, we bring a novel one-shot method to the view planning problem, *i.e.*, facing partial reconstruction but predicting a set of views from pre-learned global knowledge about object geometry.

However, when facing an unknown environment, the information about the object remains only partial, which considerably affects the prediction quality of the SCVP. Although SCVP is highly efficient for reconstruction, it struggles to capture sufficient surface details. In this work, we try to answer a crucial question: *How can we enhance the prediction quality of one-shot view planning by providing extra information about the object to be reconstructed?*

We answer this question by analyzing two solutions to providing extra information. One is to *online* provide more perception data from NBVs, *i.e.*, input with more object surfaces, as detailed in Sec. III. The other is to *offline* provide more geometric knowledge about the unknown object, *i.e.*, training from the long-tail multiview dataset instead of the singleview, as detailed in Sec. IV. Extensive experiments detailed in Sec. V validate that the integration of one-shot view planning with a single NBV through the long-tail sampling results in both high-quality and high-efficiency reconstruction.

III. PROBLEM FORMULATION AND SYSTEM OVERVIEW

We describe the view planning problem in an active vision system designed for unknown object reconstruction tasks. Subsequently, we formulate the combined pipeline that integrates one-shot view planning with NBVs. Finally, the definition of views and path planning are elucidated.

A. View Planning for Unknown Object Reconstruction

The unknown object reconstruction task considered in this work is reconstructing a high-quality 3D model of an object in an unknown and spatially limited 3D space through a sequence of sensor views navigated by a robotic arm. The six-degrees-of-freedom (6-DOF) robotic arm is equipped with an RGB-D camera at its end effector to acquire color point clouds. We adopt an OctoMap M to represent the environment and its occupancy, which is composed of three states of layered voxels, including occupied, free, and unknown voxels [33]. Our system constructs the 3D model of the object as a high-resolution color point cloud model P .

This work assumes that one side of the object surface can be seen from the initial view v_0 before reconstruction. Therefore, there is a maximum size bound to the estimated object geometry. Note that the size of the object can be arbitrary, as long as it does not exceed the field of view of the camera. The assumption is reasonable in a tabletop environment, where the size of the objects is relatively small [6].

A view in the candidate view space $V \subset \mathbb{R}^3 \times SO(3)$ of the eye-in-hand camera is 6-DOF, *i.e.*, the 3D position and the pose. The position is defined on a hemisphere around the placed object, and the pose is pointing to the center of the object, as detailed in Sec. III-C. The view planning problem is to generate the optimal sequence of views V^* that simultaneously satisfies the following two objectives: reconstruction of a high-quality point cloud model P , and efficient observation of these surfaces within short paths.

Existing solutions for the view planning problem include iterative NBV planning and one-shot view planning. Brief definitions of each are provided below:

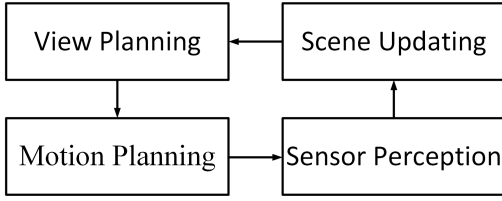


Fig. 2: Combined view planning system structure.

Definition 1: The iterative NBV view planning is to find the NBV $v_i^* \in V$, where $i \in \mathbb{N}$ is the current reconstruction iteration. The planned view sequence $V^* = \{v_0, v_1^*, v_2^*, \dots, v_i^*, \dots\}$ starts with the initial view v_0 and appends the NBV v_i^* until a stop criterion is met.

Definition 2: The one-shot view planning is to find the smallest subset $V_{cover}^* \subset V$ that can ideally cover all the remaining object surfaces, and then compute V_{path} by global path planning on V_{cover}^* (detailed in Sec. III-C). The planned view sequence $V^* = \{v_0, v_1^*, v_2^*, \dots, v_{|V_{path}|}^*\}$ starts with the initial view v_0 and appends views in V_{path} , where $||$ stands for the size of the set.

B. Combined View Planning System

To achieve a higher reconstruction quality, in this work, we propose the combined solution for view planning, which is the synthesis of the one-shot solution and the NBV solution above, defined as follows:

Definition 3: The combined view planning is to select a few NBVs until an iteration number k and then compute the global path V_{path} by one-shot view planning. The planned view sequence $V^* = \{v_0, v_1^*, v_2^*, \dots, v_k^*, v_{k+1}^*, v_{k+2}^*, \dots, v_{k+|V_{path}|}^*\}$ starts with the initial view v_0 , and appends NBVs and views in V_{path} .

To achieve this combined pipeline, we follow the typical closed-loop control process of the active vision system [5]. As shown in Fig. 2, the system comprises four modules, which are detailed as follows.

1) *View Planning:* This module takes the current environment and the candidate view space as input and outputs the NBV or the sequential global view path V_{path} , including global path planning. For the initial view v_0 , it can be a random view of the candidate view space or user-defined. For the NBV planning submodule, a variety of methods can be chosen as described in Sec. V-A. For the one-shot view planning submodule, the function of our MA-SCVP network is described in Sec. IV. To illustrate the main workflow of view planning, an example of one NBV ($k = 1$) combining our MA-SCVP network is shown in Fig. 3.

2) *Motion Planning:* This module navigates the robot to a planned view, including workspace, local path planning, and trajectory planning. The robot workspace contains the areas in which the robot can move, which depend on the robot kinematics equation [64]. For local view path planning, the obstacle avoidance method is defined in 3D space as described in Sec. III-C. For trajectory planning, the point-to-point motion is performed by the kinematics solver [65].

3) *Sensor Perception:* This module outputs the registered point cloud from the current view. For RGB-D images from the camera, we use the Default preset and the Align operation [28] to generate a high-resolution color point cloud. We use the

Algorithm 1 Combined View Planning Method

Require: Initial View v_0 , Maximum NBV Iteration k

```

1:  $V^* \leftarrow \{v_0\}$ 
2:  $MotionPlanning(v_0)$ 
3:  $P_0 \leftarrow SensorPreception(v_0)$ 
4:  $P, M, V_{state} \leftarrow SceneUpdating(P_0)$ 
5: for  $i$  from 1 to  $k$  do
6:    $v_i^* \leftarrow NBVPlanning(P, M, V_{state})$ 
7:    $V^* \leftarrow \{V^*, v_i^*\}$ 
8:    $MotionPlanning(v_i^*)$ 
9:    $P_i \leftarrow SensorPreception(v_i^*)$ 
10:   $P, M, V_{state} \leftarrow SceneUpdating(P_i)$ 
11: end for
12:  $V_{cover}^* \leftarrow f_{MA-SCVP}(M, V_{state})$ 
13:  $V_{path} \leftarrow GlobalPath(V_{cover}^* \cup \{v_k^*\})$ 
14: for  $v_{k+i}^* \in V_{path}$ ,  $i$  from 1 to  $|V_{path}|$  do
15:    $V^* \leftarrow \{V^*, v_{k+i}^*\}$ 
16:    $MotionPlanning(v_{k+i}^*)$ 
17:    $P_{k+i} \leftarrow SensorPreception(v_{k+i}^*)$ 
18:    $P \leftarrow SceneUpdating(P_{k+i})$ 
19: end for
20:  $P \leftarrow BackgroundFilter(P)$ 
21: return  $P, V^*$ 
  
```

hand-eye calibration [66] to coarsely register the point clouds. Then the iterative closest point algorithm citewang2017survey is used to finely reduce the error.

4) *Scene Updating:* This module updates the state of the environment from point clouds, including the 3D representations, the object size and center, and the candidate view space. The OctoMap updates through the default Insertion operation of a point cloud with its view. The V_{state} is a binary vector describing whether a view has been visited or not.

Algorithm 1 summarizes the auto-stop object reconstruction procedure based on the combined view planning system. The number $k \in \mathbb{N}$ of the maximum NBV iteration is studied in Sec. V-D. Note that $k = 0$ means no NBV selected and performs directly one-shot view planning with the initial view v_0 . This work assumes that there is only one object to be reconstructed in a tabletop scenario. Therefore, at the end of the reconstruction process, the 3D point cloud model can be obtained by filtering the background of the table (line 20) by the height or a filtering method [67]. It is worth mentioning that the OctoMap M does not need updates during Scene Updating in the global path execution (line 18) because the 3D model is constructed using point clouds. This reduction in the number of OctoMap updates contributes to the computation speed of our system, as detailed in Sec. V-E.

C. View Path Planning

Here we define the candidate view space before presenting the view path planning. The position of the candidate views is defined by Spherical Codes [68], which solves the problem of placing a few points on a sphere to maximize the minimal distance between them. This helps to minimize the intersection of perception on views. Given our focus on the tabletop scenario, only views on the upper hemisphere are considered. Note that in real-world applications, the radius of the view

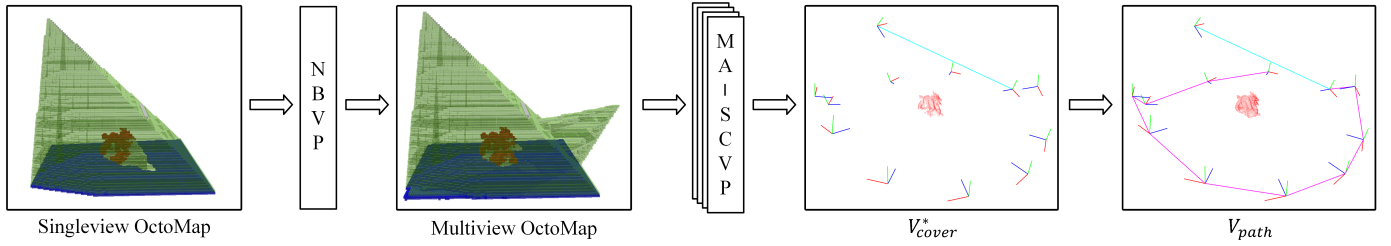


Fig. 3: Illustration of the combined view planning pipeline, which performs one NBV planning (NBVP) before activating the MA-SCVP network: The inputs are displayed in OctoMaps to clearly show free areas (green), occupied areas (red object and blue table), and unknown areas (gray voxels near the object). In brief, point clouds and view states are not shown here, which may be required by some view planning methods. The partially reconstructed object models are shown in point cloud space as well as views (red-green-blue), local paths (cyan), and global paths (purple). The output V_{cover}^* is the predicted smallest subset covering the remaining object surfaces (views excluding two visited views), which is sequenced to V_{path} by global path planning.

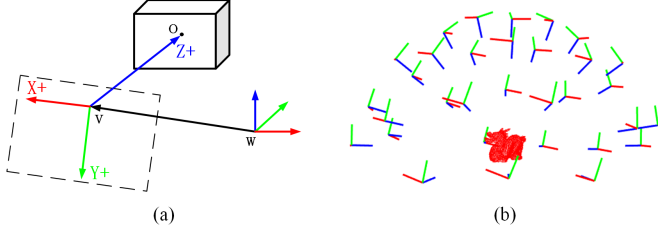


Fig. 4: Illustration of candidate views: (a) The 5-DOF view pose. The last DOF can be regarded as rotating the view pose along the Z+ by any degree (rotating the XvY plane, black rectangle). (b) The view space of 32 candidates.

space sphere may vary according to the size of the object because the RGB-D camera needs a certain distance from the object to obtain correct depth images.

The pose of each candidate view is defined as pointing to the center of the object, which is similar to NBVNet [10]. Assume that $o(o_x, o_y, o_z)$ is the object center position, $v(v_x, v_y, v_z)$ is the view position, and $w(w_x, w_y, w_z)$ is the origin of world coordinate system. Thus, we define that Z+ (our camera points along the Z+ axis) is $\vec{v}o$ (units into r_z), the Y+ of the view pose is $\vec{v}o \times \vec{w}v$ (units into r_y), and the X+ of the view pose is $r_x = r_y \times r_z$. The homogeneous view matrix H_v is defined as:

$$H_v = \begin{pmatrix} r_x & r_y & r_z & 0 \\ 0 & 0 & 0 & 1 \end{pmatrix}^{-1} * \begin{pmatrix} I & -\vec{w}v \\ 0 & 1 \end{pmatrix} \quad (1)$$

As discussed in NBVNet [10], pointing to the center of the object defines the 5-DoF pose, and the last degree of freedom has almost no effect on the reconstruction. We illustrate this 5-DoF definition in Fig. 4(a) and many 6-DoF poses are valid here. In general, the last degree of freedom can be chosen as the most upward camera pose or a pose with minimal change from the previous pose. It is worth mentioning that in real-world applications, as the reconstruction proceeds, the size and the center of the object change. Therefore, our view pose also adapts to the change, and the effects are studied in Sec. V-F.

The size $|V|$ of the candidate view space is set to 32 as in our previous work SCVP [6]. In most cases, having 32 views on the upper hemisphere in a tabletop scenario is sufficient to observe all visible areas. This choice is influenced by the fact that NBVNet [10] assumes 14 views on the upper hemisphere, while PCNBV [8] assumes 33 views on the whole sphere. We illustrate the candidate view space in Fig. 4(b).

1) *Local View Path Planning*: A local view path is a path between two views. To navigate the robot arm from one view to another, we need to consider the obstacles of the object and the tabletop. For safety reasons, we define an obstacle as

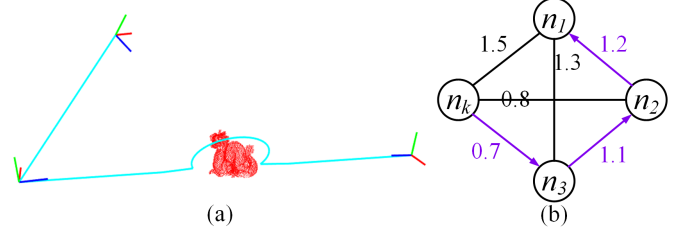


Fig. 5: Illustration of the view path planning: (a) local path planning (cyan) of a straight path and an obstacle avoidance path; (b) global path planning (purple) by finding the shortest Hamiltonian path on the undirected complete graph of views.

a bounding sphere around the object, where the center is the center of the object and the radius is the size of the object. We can ignore the tabletop because the candidate views are all above it. Formally, the local path length between any two views is given as:

$$Path(v_i, v_j) = \begin{cases} \|v_i - v_j\|^2, & \text{if } rt_1 \text{ or } rt_2 \text{ does not exist} \\ \|v_i - rt_1\|^2 + Arc(rt_1, rt_2) + \|rt_2 - v_j\|^2, & \text{else} \end{cases} \quad (2)$$

where $\|\cdot\|^2$ is the Euclidean distance between the 3D positions of two views, rt_1, rt_2 are the two intersection points between the obstacle sphere and the 3D line, and $Arc(rt_1, rt_2)$ is the arc length on the sphere. In most cases, the arc is above the object and computes as the spherical distance, *i.e.*, the length of the minor arc of the great circle. In the case of the minor arc below the object, we instead use the major arc to avoid collisions. As shown in Fig. 5(a), if there is no obstacle, the local path will be straight, otherwise, it will go around it. We next sample some points on the local path and traverse them with better trajectory planning.

2) *Global View Path Planning*: The global path consists of some local paths between a set of views. The goal of global path planning is to find the shortest local paths to traverse all the views, formally defined as:

Definition 4: Given the set of views $V_{cover}^* \cup \{v_k^*\}$ and the local path between any two views, the global path planning problem is to find the sequence V_{path} , whose total path length $\sum_{i=1}^{|V_{cover}^*|} Path(v_i, v_{i+1})$ is minimized. Note that the sequence starts from the current view v_k^* , *i.e.*, $v_1 = v_k^*$.

This problem is known as the shortest Hamiltonian path problem, which is similar to the traveling salesman problem but without returning to the starting point [69]. A Hamiltonian path is a path in an undirected graph that visits each vertex exactly once. Note that here the path is a set of edges in the

graph. The shortest Hamiltonian path is a Hamiltonian path with minimized total distance weight of edges.

To define it, we generate an undirected complete graph $G = (N, E)$, whose vertex $n_i \in N$ is the view $v_i \in V_{cover}^* \cup \{v_k^*\}$, and whose edge $\langle n_i, n_j \rangle \in E$ has a distance weight of the local path length $Path(v_i, v_j)$. The global path planning problem is now to find the shortest Hamiltonian path from the vertex $n_k (v_k^*)$ to another vertex. Fig. 5(b) shows an example of the shortest Hamiltonian path between vertices n_k and n_1 , which has a minimum total distance 3.0 of edges.

Solving the shortest Hamiltonian path is known to be NP-hard, but state compression dynamic programming [69] can be used to solve it with time complexity $O(n^2 2^n)$. Since the number of vertices is usually not more than 20, it can be solved in an acceptable time (much less than a second).

IV. LEARNING ONE-SHOT VIEW PLANNING VIA LONG-TAIL MULTIVIEW SAMPLING

This section introduces the network function $f_{MA-SCVP}$ in Algorithm 1 (line 12), responsible for predicting the smallest subset V_{cover}^* that covers the remaining object surfaces. First, we discuss the long-tail distribution phenomena related to surface coverage gain and propose the long-tail sampling method to create multiview input cases. Second, the SCOP is defined for these input cases to create our long-tail view-planning dataset. Finally, we propose the multiview-activated SCVP network architecture to enhance training performance.

A. Long-Tail Sampling of Multiview Input Cases

An input case (c_{obj}, c_{view}) for our network is defined as a pair of object case and view case, where $c_{obj} = (o, r)$ comprises an object o with its rotation angle r , and $c_{view} \in (0, 2^{32})$ is an integer. The binary bits of c_{view} indicate whether a candidate view is selected or not. The multiview OctoMap in Fig. 3 illustrates an example of a multiview input case. Specifically, the object case is the Dragon object placed at a certain rotation angle on the tabletop, while the view case consists of two 1 bits representing an initial view and an NBV. The partially reconstructed data that serve as input to our network are determined by this case. In other words, one input case can only generate a partially reconstructed object OctoMap, and vice versa.

1) *Traditional Input Case Sampling*: Since c_{obj} is easy to determine, a straightforward sampling method is to random sample a set of c_{view} . However, this method fails to obtain valuable data for view planning. Fig. 6(a) shows the binomial distribution of the number of c_{view} over the number of selected views in each c_{view} (the total number of 1 bit). Random sampling from this distribution results in a concentration of 14-18 selected views that is enough to cover most of the object surfaces, making the data useless for view planning. In more extreme cases, where 20 or more selected views cover the entire surface, the need for view planning is eliminated entirely, *i.e.*, no views can be labeled for these input cases.

Therefore, instead of direct random sampling, existing NBV networks [8], [10], [56], [58] employ the NBV-reconstruction (NBVR) sampling method. This traditional method performs several simulated NBV reconstruction trials on different c_{obj} ,

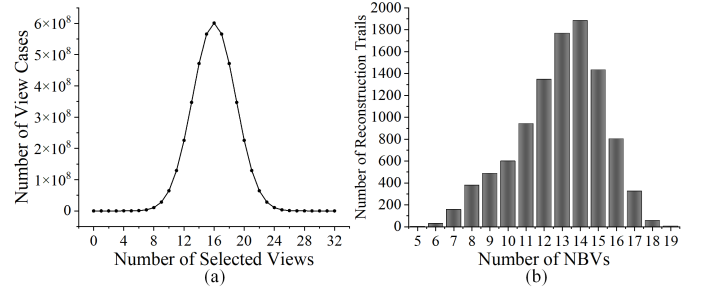


Fig. 6: Unsuitability of random sampling: (a) Distribution of the number of view cases over the number of selected views. (b) Distribution of the number of reconstruction trails over the number of NBVs for achieving 100% surface coverage. These two distributions illustrate that random sampling results in many input cases with already full coverage, rendering them unable to have any views labeled.

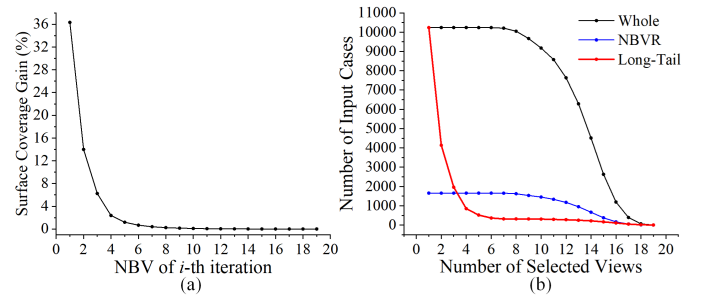


Fig. 7: Long-tail phenomenon and sampling methods: (a) Distribution of the surface coverage gain over the NBV corresponding to the i -th iteration. Note that the coverage of the initial view (iteration 0) is not relevant and omitted here, which is about 38.02%. (b) Distributions of the number of sampled input cases over the number of selected views, where Whole stands for the whole sampling space while NBVR and Long-Tail denote two sampling methods. The importance of an input case is assessed by the surface coverage gain of its NBV. Therefore, we design the long-tail sampling method to align with the characteristic long-tail curve shape.

recording each c_{view} in each iteration until achieving full coverage of object surfaces. It is reasonable to consider only NBVs in c_{view} because a well-trained network is assumed to work on the input of ideal NBV perception data.

As it guarantees that each input case has at least one view to be labeled, we also follow the NBV reconstruction process to construct our whole sampling space C_{whole} as detailed in Appendix A. Along with constructing C_{whole} , we depict how many NBVs are required to finish these objects in Fig. 6(b). The results confirm that most objects in reconstruction trials require 12-15 NBVs for 100% coverage, indicating the unsuitability of random sampling.

2) *Distribution of Surface Coverage Gain*: Although each input case in C_{whole} can be utilized for network training, their importance varies. For instance, a 15-view input case may already cover 97% surfaces, making it less valuable. Therefore, a natural question arises: *how many NBVs are needed to cover most portion (e.g., 80%) of the object surfaces?*

Fig. 7(a) calculates the surface coverage gain of the NBV corresponding to the i -th iteration, revealing a classic long-tail distribution frequently observed in deep learning [9]. It illustrates that the first 1-3 views (an initial view and 2 NBVs) cover more than 80% of the object surfaces, while subsequent views only contribute to the remaining 20%. Intuitively, an input case with fewer selected views should be considered more important. In other words, we need to prioritize sampling

Algorithm 2 Long-Tail Input Case Sampling Method

Require: *Whole Input Cases* C_{whole}

- 1: $RandomShuffle(C_{whole})$
- 2: **for all** $(c_{obj}, c_{view}) \in C_{whole}$ **do**
- 3: $n_{select} \leftarrow PopCount(c_{view})$
- 4: **if** $|C_{(c_{obj}, n_{select})}| < L(c_{obj}, n_{select})$ **then**
- 5: $C_{(c_{obj}, n_{select})} \leftarrow C_{(c_{obj}, n_{select})} \cup \{(c_{obj}, c_{view})\}$
- 6: **end if**
- 7: **end for**
- 8: **for all** c_{obj} **do**
- 9: **for** n_{select} **from** 1 **to** $|V|$ **do**
- 10: $C_{longtail} \leftarrow C_{longtail} \cup C_{(c_{obj}, n_{select})}$
- 11: **end for**
- 12: **end for**
- 13: **return** $C_{longtail}$

more input cases with fewer selected views.

3) *Long-Tail Sampling Method:* We thereby design a long-tail sampling method to make our sampled distribution the long-tailed shape curve. Our method is summarized as Algorithm 2. *RandomShuffle* is used to randomly sort the set (line 1). We denote n_{select} as the number of selected views in c_{view} , which is easy to obtain by *PopCount* operation counting 1 bit (line 3). Given the fact that each object case c_{obj} has its own long-tail distribution because objects can vary in size, occlusion, and surface complexity. Thus, we tailor the number of maximum sampled cases $L(c_{obj}, n_{select})$ for each object:

$$L(c_{obj}, n_{select}) = \begin{cases} n_{single}, & n_{select} = 1 \\ \lceil n_{single} \times \frac{NS(c_{obj}, n_{select})}{NS(c_{obj}, 1)} \rceil, & n_{select} \neq 1 \end{cases} \quad (3)$$

where $n_{single} \in [1, 32]$ is a user-defined integer of single-view cases to control the total number of samples (by default, $n_{single} = 32$ equals the number of candidate views). $NS(c_{obj}, n_{select})$ is the surface coverage gain of the object c_{obj} under n_{select} -th NBV. The detailed computation of $NS(c_{obj}, n_{select})$ can be found in Appendix A. We apply the ceiling operation to ensure that there is at least one case for any number of selected views. It is worth mentioning that we generate datasets using different n_{single} as it changes the long-tailed shape, as detailed in Sec. V-B.

To illustrate our long-tail sampling method, we plot the number of sampled input cases over the number of selected views shown in Fig. 7(b). The black curve represents the distribution of C_{whole} , where it gradually goes to zero due to the different number of NBVs required for full coverage. The red curve illustrates our distribution of $C_{longtail}$, characterized by a long-tail shape. Additionally, the blue curve shows the distribution of C_{nbvr} from the NBVR sampling method, sharing a similar shape with the C_{whole} as it uses uniform sampling. We validate the superiority of our long-tail sampling over the NBVR sampling method in Sec. IV-B and IV-C.

B. Multiview Dataset Generation through SCOP

Given multiview input cases from $C_{longtail}$, our goal is to automatically generate the view planning dataset by solving SCOP and considering sim-to-real gaps.

Algorithm 3 View Planning Dataset Generation

Require: *Long-Tail Input Cases* $C_{longtail}$

- 1: **for all** $(c_{obj}, c_{view}) \in C_{longtail}$ **do**
- 2: **for all** $v \in V$ **do**
- 3: $\mathbb{v} \leftarrow VirtualImaging(c_{obj}, v)$
- 4: $U \leftarrow U \cup \mathbb{v}$
- 5: **end for**
- 6: $V_{state} \leftarrow Decompress(c_{view})$
- 7: $M \leftarrow Initialize\ with\ Tabletop$
- 8: **for all** $v = 1 \wedge v \in V_{state}$ **do**
- 9: $M \leftarrow Insert\ with\ \mathbb{v}$
- 10: $U_{cover} \leftarrow U_{cover} \cup \mathbb{v}$
- 11: **end for**
- 12: $U_{rest} \leftarrow U \setminus U_{cover}$
- 13: **for all** $v \in V$ **do**
- 14: $\mathbb{v}_{rest} \leftarrow \mathbb{v} \setminus U_{cover}$
- 15: $\mathbb{V}_{rest} \leftarrow \mathbb{V}_{rest} \cup \mathbb{v}_{rest}$
- 16: **end for**
- 17: $V_{label}^* \leftarrow SetCoveringOptimizer(U_{rest}, \mathbb{V}_{rest})$
- 18: $Save(M, V_{state}, V_{label}^*)$
- 19: **end for**

1) *Automatic Dataset Generation:* Algorithm 3 summarizes the automatic dataset generation process, which is visualized in Fig 8. The virtual imaging is performed for each candidate view to obtain the set \mathbb{v} of object voxels observed from a view v (line 4) and the set U of all visible object voxels (line 5). The view state V_{state} is easy to obtain by decompressing the bits of c_{view} (line 6). The OctoMap M for the network input is initialized to unknown voxels and inserted with a set of occupied voxels representing the tabletop (line 7). Then the OctoMap M is inserted with the observed voxels from each selected view in V_{state} (line 9). U_{cover} can be obtained by the union of all observed object voxels (line 10). Next, the rest universe set U_{rest} is all the uncovered object voxels removing those observed voxels (line 12). A collection of rest view sets \mathbb{V}_{rest} is the union of each view set \mathbb{v} removing those observed voxels (lines 14-15). Finally, the smallest set V_{label}^* is solved by the set-covering optimizer (line 17), and the supervision pair $(M, V_{state}, V_{label}^*)$ is stored in the view planning dataset (line 18). Note that Algorithm 3 is designed to generate a view planning dataset for set covering, but it is easy to modify lines 12-17 by $v^* \leftarrow \arg \max_v |\mathbb{v} \setminus U_{cover}|$ to generate a view planning dataset for NBV planning.

2) *Labeling through SCOP:* The function of the set-covering optimizer (line 17) is to find the smallest set V_{label}^* that fully covers the remaining object surfaces U_{rest} . To give an intuitive understanding of the smallest set of views, Fig. 9 illustrates the surfaces of the Cat object, representing coverage from different views with distinct colors. It shows that eight views are required to cover all object surfaces. For example, if the black and red views are selected in the input case, the V_{label}^* then becomes the set of six remaining views. The problem of finding the smallest set V_{label}^* is transformed into a class of set covering optimization problems (SCOP):

Definition 5: Given the universe set U_{rest} of all uncovered object voxels and the collection \mathbb{V}_{rest} of all view sets removing observed voxels, SCOP for labeling one-shot view planning is

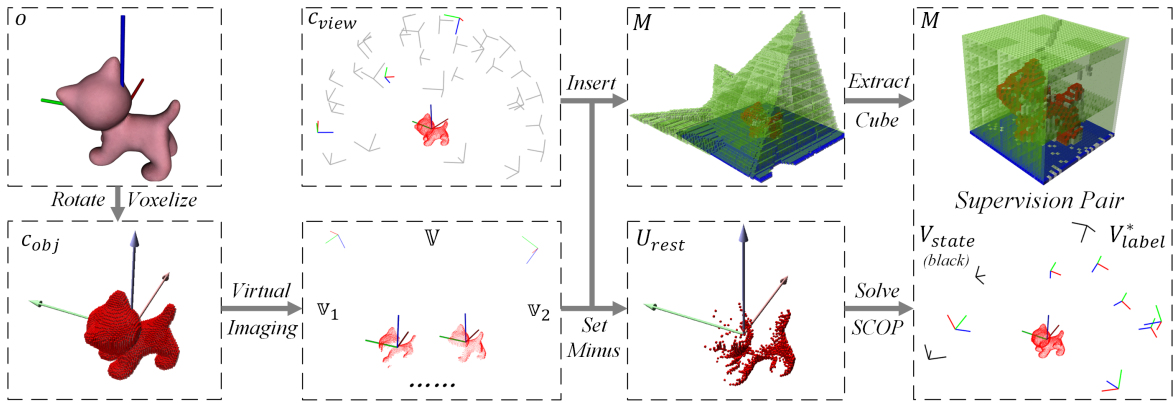


Fig. 8: Illustration of the visual steps of view planning dataset generation for set covering. c_{obj} is generated from the mesh model o and a rotation angle r . c_{view} is the selected views in the candidate view space and decompressed to V_{state} . Taking a certain input case of (c_{obj}, c_{view}) , the collection \mathbb{V} of all view sets can be obtained by virtual imaging. The input OctoMap M is the squared grid obtained from the observations of the selected views in V_{state} . The smallest set V_{label}^* is solved by SCOP, covering the rest universe set U_{rest} obtained by removing the covered voxels of selected views in V_{state} .



Fig. 9: Set covering for view planning: colors represent views and the surfaces they cover.

to find the sub-collection of \mathbb{V}_{rest} with the smallest number w of view sets, whose union equals the universe U_{rest} .

For instance, consider the universe set $U_{rest} = \{1, 2, 3, 4, 5\}$ and the collection $\mathbb{V}_{rest} = \{v_1 = \{1, 2, 3\}, v_2 = \{2, 3, 4\}, v_3 = \{1, 4, 5\}\}$. Clearly, the union of \mathbb{V}_{rest} is U_{rest} ($v_1 \cup v_2 \cup v_3 = U_{rest}$). However, we can cover all voxels with a smaller number of sets, $w = 2: \{v_2, v_3\}$. Thus, $V_{label}^* = \{v_2, v_3\}$ can be obtained.

SCOP has a long history in operations research [70]. It is an NP-hard problem and is usually defined as an integer linear program (ILP) expression:

$$\begin{aligned} \text{minimize: } & \sum_{v \in \mathbb{V}_{rest}} z_v \\ \text{subject to: } & (a) \sum_{\mathbb{V}_{rest}: e \in v} z_v \geq 1 \text{ for all } e \in U_{rest} \\ & (b) z_v \in \{0, 1\} \text{ for all } v \in \mathbb{V}_{rest} \end{aligned} \quad (4)$$

The objective function $\sum_{v \in \mathbb{V}_{rest}} z_v$ is to minimize the number of chosen view sets. It is subject to (a) each voxel element $e \in U_{rest}$ must be covered by at least one chosen view that can observe this voxel ($e \in v$), and (b) each view set is either in the collection of chosen sets or not.

The ILP expression of SCOP makes it solvable by a linear programming solver. We choose Gurobi Optimizer to solve SCOP, which takes the lead in the benchmark of linear programming solvers [71]. Since the problem size of SCOP is not too large (the number of voxels and views is not too many), Gurobi can solve SCOP in an acceptable time for labeling (less than 10 seconds).

3) *Sim-to-Real Gaps*: To bridge the gap between the input cases in the simulation and the real-world situation, three issues should be considered:

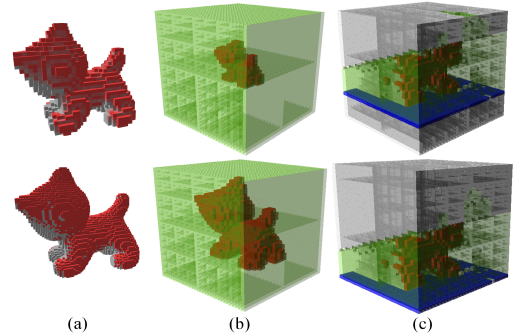


Fig. 10: Sim-to-real gap improvements: (a) Imaging resolution 0.004 m (top) vs. 0.002 m (bottom). (b) Fixed resolution (top) vs. Dynamic (bottom). (c) Grid of the object center (top) vs. Bottom of the tabletop (bottom).

Resolution for virtual imaging. The resolution of the OctoMap for the virtual imaging determines the performance of SCOP because the U_{rest} and \mathbb{V}_{rest} depend on the voxel size. In general, the higher the resolution (the smaller the voxel size), the better the surface details as well as the more views in V_{label}^* . It is natural to use a high resolution since our view planning goal is to achieve an object model with complete surfaces. However, there is some noise in real point clouds from an RGB-D camera whose resolution is about 0.001 m. Reducing the resolution of OctoMap can effectively reduce the noise in the point cloud. Therefore, we choose a balanced OctoMap resolution of 0.002 m for virtual imaging instead of 0.004 m in SCVP. As shown in Fig. 10(a), higher resolution OctoMap can capture more surface details.

Different sizes of objects. The size o_{size} of an object is defined as the radius of the minimum bounding sphere of the object. In SCVP, we resized objects from 3D model datasets to a maximum size of 0.10 m and used a fixed resolution of 0.00625 m of the OctoMap M for the network input (note that this is not the OctoMap used for virtual imaging). However, some objects with a small original size (such as 0.05 m) can only occupy half of the OctoMap. In this study, we adopt a dynamic resolution of $M_{res} = 2 \times o_{size}/32$. The resolution is calculated this way because the OctoMap M is eventually divided into a cube grid whose edge length is twice the size o_{size} of an object. As shown in Fig. 10(b), the small object will lose surface details in a fixed resolution of OctoMap.

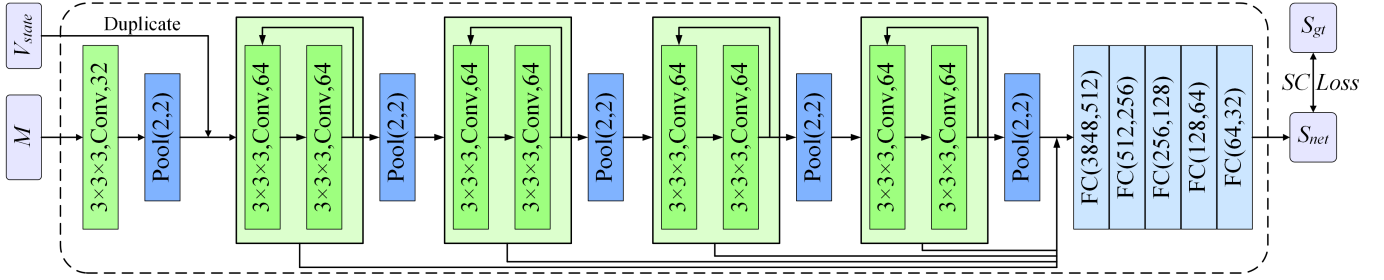


Fig. 11: MA-SCVP network architecture: Conv block denotes 3D convolution operation with Batch Normalization (BN) [72] and Leaky Rectified Linear Units (ReLU) [73]. Pool denotes Max-Pooling. FC denotes fully connected layers. The intersections of these arrows denote the concatenate operation of features.

Furthermore, this allows our network inputs to no longer be limited by the size of the object.

Tabletop. In real-world situations, an object is placed on a tabletop. To combine the OctoMap M with the tabletop information, we insert a tabletop plane immediately below the object. In SCVP, the center of the divided grid of the OctoMap M is set to the object center. However, the tabletop will have an unfixed position since objects vary in height. In this work, we move down the grid center to make sure the tabletop is fixed at the bottom of the grid as shown in Fig. 10(c).

C. Multiview-Activated SCVP Network Architecture

The function of the multiview-activated MA-SCVP network is a classic multilabel classification [74] function:

$$f_{MA-SCVP}(M, V_{state}) : \mathbb{R}^{32 \times 32 \times 32} \times \{0, 1\}^{32} \rightarrow \{0, 1\}^{32} \quad (5)$$

This function takes a $32 \times 32 \times 32$ occupancy grid and a vector of 32 bits as input and predicts a vector of 32 bits so that the V_{cover}^* can be obtained.

We follow the setting in NBVNet [10] to construct the shape size of our input and output. Since convolution is easier to operate on data with equal dimensions, we extract a $32 \times 32 \times 32$ cubic bounding box of the object from the OctoMap M . We adopt the dynamic resolution of M so that the shape size of $32 \times 32 \times 32$ is sufficient to generalize to different object sizes. In the real world, we assume o_{size} is not greater than 15 cm, which can be predicted by solving the minimum bounding sphere (bounding box) in the point clouds to obtain the M . The view state vector V_{state} is the same size as our candidate view space. A bit in our network output is bound to a certain candidate view because the SCOP is solved in such a fixed candidate view space. The challenge of a fixed view space with varying rotations of objects is addressed through training based on multiple rotations r .

1) *View State and MA-SCVP Network:* To learn from multiview input data, it is necessary to handle the view state vector input to the deep network. The view state inputs information about previously visited views into the network, reducing the likelihood of predicting views that have already been visited. As demonstrated in PCNBV [8], using the view state as input leads to better predictions of views.

Fig. 11 shows the architecture of the MA-SCVP network. After extracting features from the original grid once (1 Conv), we duplicate the view state vector 32 times before the concatenate operation to make the features structured, which is similar to PCNBV [8]. Then four convolution-based blocks are used to extract features at different resolutions. We apply

residual learning to each block (2 Conv blocks have two skip connections) because it will be easy to optimize as shown in the literature [75]. Before putting the features into five fully connected layers, we concatenate the features extracted at four resolutions so that they will have a multi-resolution horizon. In particular, the 3D features are concatenated at channel dimension and then flattened to fully connected layers. Finally, the final score for each candidate view is computed into a vector of 32 real numbers, S_{net} .

2) *Loss Function:* The $SCLoss$ function is proposed to calculate the difference between S_{net} and S_{gt} . The $S_{gt} = \{s_i | s_i = 1 \text{ if } v_i \in V_{label}^* \text{ or } s_i = 0 \text{ if } v_i \notin V_{label}^*\}$ is the binary ground truth mask of V_{label}^* . We define the $SCLoss$ with aid of the cross-entropy loss term widely used in deep learning:

$$CE_i = s_i^{gt} \log s_i^{net} + (1 - s_i^{gt}) \log(1 - s_i^{net}) \quad (6)$$

where $s_i^{net} \in S_{net}$ is the predicted score and $s_i^{gt} \in S_{gt}$ is the ground truth mask. As shown in SCVP [6], the 1's and 0's in the ground truth mask S_{gt} have different importance to the network training. We use a hyper-parameter λ to balance them:

$$SCLoss = -\frac{1}{32} \sum_i [(1 - s_i^{gt}) \times CE_i + \lambda \times s_i^{gt} \times CE_i] \quad (7)$$

The value of λ depends on the distribution of 1's in the ground truth masks of a certain view planning dataset.

3) *Network Output:* The output of the network is a vector of 32 bits computed by a parameter γ . For each view score $s_i \in S_{net}$, we mark the view score greater than γ as 1, otherwise 0. Formally, the final predicted view subset V_{cover}^* is defined as $\{v_i | s_i > \gamma \wedge v_i \in V\}$. It is natural to set $\gamma = 0.5$ as a common confidence threshold for classification problems since we have no prior knowledge before training. Moreover, we experimentally validate parameters λ and γ in Appendix B-A.

V. EXPERIMENTAL RESULTS

Extensive simulation experiments are designed to support our claims that: (1) the long-tail sampling method enhances both the network training (Sec. V-B) and the reconstruction test (Sec. V-C); (2) the MA-SCVP network trained on our long-tail multiview dataset enhances the reconstruction quality with less number of required NBVs compared to the SCVP network trained on the singleview dataset (Sec. V-D); (3) our system achieves concurrently high-quality and high-efficiency reconstruction of unknown objects compared to state-of-the-art systems (Sec. V-E). Next, we provide real-world experiments to validate the generalization and deployment of our system

Network	Dataset	Recall (%)	Precision (%)	F_1 (%)
OctreeNet [80] w/o view state	NBVR-8K	75.87	69.39	72.49
	Long-Tail-8K	68.13	72.60	70.29
	NBVR-20K	80.50	74.54	77.41
	Long-Tail-20K	81.48	82.45	81.96
OctreeNet [80] w/ view state	NBVR-8K	77.10	81.00	79.00
	Long-Tail-8K	67.84	70.65	69.22
	NBVR-20K	79.98	77.44	78.69
	Long-Tail-20K	82.40	81.45	81.92
MA-SCVP w/o view state	NBVR-8K	68.27	50.47	58.04
	Long-Tail-8K	79.60	57.69	66.90
	NBVR-20K	72.37	59.04	65.03
	Long-Tail-20K	86.13	76.23	80.88
MA-SCVP w/ view state	NBVR-8K	73.62	75.03	74.32
	Long-Tail-8K	74.31	74.21	74.26
	NBVR-20K	80.26	84.29	82.22
	Long-Tail-20K	83.95	85.76	84.84

TABLE I. Evaluation of network architecture and dataset on training metrics: Each metric value is computed on the validation set. **w/** stands for with, while **w/o** stands for without. As can be seen, our MA-SCVP with view state trained on the Long-Tail-20K dataset achieves the highest F_1 score, indicating superior network performance.

long-tail samples, resulting in 20,740 and 7,962 samples, denoted as Long-Tail-20K and Long-Tail-8K, respectively. As NBVR samples are dynamically obtained by the number of initial views, we generate a comparable number of samples, totaling 20,952 and 8,281, denoted as NBVR-20K and NBVR-8K, respectively. It takes around 25 hours to generate the Long-Tail-20K dataset. Our datasets can be found on <https://www.kaggle.com/datasets/sicongpan/ma-scvp-dataset>.

2) *Training Details*: To explore the effectiveness of multiview-activated architecture, we examine our MA-SCVP networks with and without the input of the view state. We employ the Adam optimizer [81] with a base learning rate set at 0.0004 and a mini-batch size of 8. The networks undergo training for 300 epochs. The parameters λ and γ are examined in Appendix B-A.

3) *Metrics and Results*: We used two metrics to evaluate the network performance:

$$Recall = \frac{|V_{true}^*|}{|V_{label}^*|}, Precision = \frac{|V_{true}^*|}{|V_{cover}^*|} \quad (11)$$

where $V_{true}^* = \{v|v \in V_{cover}^* \wedge v \in V_{label}^*\}$ is the set of predicted views that are also correct in the label. A low-recall network will miss some views that greatly improve coverage while a low-precision network will have redundancy of predicted views. The F_1 score is used to balance these two metrics:

$$F_1 = \frac{2 \times Recall \times Precision}{Recall + Precision} \quad (12)$$

In addition to our MA-SCVP networks, we conduct a comparison with OctreeNet [80], a recent architecture designed for voxel grid processing. The results are reported in Table I. From the results, we have three major findings:

- The datasets with a larger sample size, 20K, generally outperform the datasets with a smaller number, 8K. This encourages us to maximize n_{single} to 32.
- The Long-Tail datasets generally outperform the NBVR datasets. This confirms our long-tail sampling method enhances the network training.
- The MA-SCVP with view state generally outperforms other architectures. This confirms our architecture enhances the network training.

Iterations	PCNBV citezeng2020pc		NBVNet [10]	
	Long-Tail	NBVR	Long-Tail	NBVR
0	38.16 \pm 7.55	38.16 \pm 7.55	38.16 \pm 7.55	38.16 \pm 7.55
1	71.90 \pm 8.63	71.49 \pm 8.77	71.01 \pm 9.12	70.09 \pm 9.57
2	85.68 \pm 5.98	85.32 \pm 6.14	84.06 \pm 7.29	82.83 \pm 7.92
3	91.40 \pm 4.93	91.14 \pm 4.87	89.47 \pm 6.52	88.74 \pm 6.99
4	93.65 \pm 4.03	93.83 \pm 3.74	91.90 \pm 5.84	91.44 \pm 6.21
5	94.74 \pm 3.46	95.34 \pm 3.04	93.41 \pm 5.23	93.15 \pm 5.54
9	96.44 \pm 2.51	97.20 \pm 2.28	95.78 \pm 3.97	96.01 \pm 4.42
14	97.20 \pm 2.15	97.65 \pm 2.05	96.44 \pm 3.81	97.05 \pm 4.00
19	97.54 \pm 1.98	97.85 \pm 1.96	96.60 \pm 3.78	97.29 \pm 3.97

TABLE II. Evaluation of NBV networks trained on datasets using different sampling methods: Each value is the mean VSC value with its standard deviation, computed over 3,000 tests. VSC stands for visible surface coverage. As can be seen, NBV networks trained on the Long-Tail dataset achieve higher coverage in early iterations.

Dataset	RV	VSC (%)	MC (m)
NBVR	14.22 \pm 2.13	98.06 \pm 4.50	2.83 \pm 0.33
Long-Tail	13.13 \pm 1.43	98.10 \pm 3.73	2.59 \pm 0.23

TABLE III. Evaluation of our MA-SCVP networks trained on datasets using different sampling methods: Each value is the mean value and its standard deviation, computed over 3,000 tests. **RV**, **VSC**, and **MC** stand for the number of required views, visible surface coverage, and movement cost, respectively. As can be seen, MA-SCVP trained on the Long-Tail dataset achieves better VSC, while notably reducing RV and MC, especially smaller standard deviation.

Based on these findings, we proceed with experiments using 20K datasets and architectures with view state. Therefore, the following MA-SCVP refers to MA-SCVP with view state, the following NBVR dataset refers to NBVR-20K, and the following Long-Tail dataset refers to Long-Tail-20K.

C. Reconstruction Study on Sampling Method

To further study the effectiveness of sampling methods, we conduct reconstruction tests on two NBV networks (PCNBV and NBVNet) and our MA-SCVP network. The NBV networks are trained following the parameters in their paper.

1) *Performance of NBV Networks*: As shown in Fig. 6, all objects received full coverage below 20 ground-truth NBVs. To test NBV networks thoroughly, Table II reports the results of NBV networks for the major iterations where $RV = 20$. From the results, we find that, in early iterations (1-4 for PCNBV and 1-5 for NBVNet), networks trained on the Long-Tail dataset exhibit higher surface coverage than those trained on the NBVR dataset. In subsequent iterations, the opposite trend is observed.

Based on this finding, we conclude that the long-tail sampling method is well-suited for NBV networks in our system, particularly since we utilize NBVs in early iterations. Therefore, the NBV networks in the following study on combined pipelines are trained on the Long-Tail dataset.

2) *Performance of MA-SCVP Network*: Since our MA-SCVP network has the auto-stop criterion, the results of the final reconstruction are reported in Table III. From the results, we find that MA-SCVP trained on the Long-Tail dataset achieves higher quality and efficiency of reconstruction than that trained on the NBVR dataset.

Based on this finding, we conclude that the long-tail sampling method improves the reconstruction performance of our MA-SCVP network, enhancing our system performance.

D. Reconstruction Study on Combined Pipeline

To establish our combined pipeline, three components require examination: (1) the selected NBV method for our

Iterations	PCNBV [8]	NBVNet [10]	RSE [7]	APORA [48]	MCMF [49]	GMC [50]
0	38.16 ± 7.55	38.16 ± 7.55	38.16 ± 7.55	38.16 ± 7.55	38.16 ± 7.55	38.16 ± 7.55
1	71.90 ± 8.63	71.01 ± 9.12	68.29 ± 10.37	64.67 ± 9.34	64.12 ± 10.09	64.19 ± 10.07
2	85.68 ± 5.98	84.06 ± 7.29	77.09 ± 9.32	76.02 ± 8.00	80.86 ± 8.70	80.90 ± 8.63
3	91.40 ± 4.93	89.47 ± 6.52	84.09 ± 7.93	83.90 ± 6.67	88.23 ± 6.53	88.43 ± 6.20
4	93.65 ± 4.03	91.90 ± 5.84	88.32 ± 6.68	88.98 ± 5.67	92.18 ± 4.97	92.41 ± 4.65
5	94.74 ± 3.46	93.41 ± 5.23	91.52 ± 5.86	91.86 ± 4.70	94.42 ± 3.83	94.65 ± 3.50
6	95.39 ± 3.08	94.33 ± 4.80	93.68 ± 5.27	93.71 ± 4.11	95.85 ± 2.86	96.03 ± 2.61
9	96.44 ± 2.51	95.78 ± 3.97	96.82 ± 3.21	96.74 ± 2.83	97.93 ± 1.68	97.95 ± 1.58
14	97.20 ± 2.15	96.44 ± 3.81	98.26 ± 1.64	98.59 ± 1.36	99.02 ± 1.07	98.93 ± 1.09
19	97.54 ± 1.98	96.60 ± 3.78	98.95 ± 0.98	99.24 ± 0.84	99.48 ± 0.75	99.33 ± 0.81

TABLE IV. Evaluation of different NBV methods to identify the most effective approach in early iterations: Each value is the mean VSC value with its standard deviation, computed over 3,000 tests. VSC stands for visible surface coverage. As can be seen, PCNBV exhibits superior performance in the early iterations (1-5), making it our final choice.

k NBV Combined	SCVP (singleview dataset) [6]			MA-SCVP (long-tail multiview dataset)		
	RV	VSC (%)	MC (m)	RV	VSC (%)	MC (m)
0	9.61 ± 0.96	96.12 ± 6.29	2.28 ± 0.15	13.13 ± 1.43	98.10 ± 3.73	2.59 ± 0.23
1	10.24 ± 1.03	96.99 ± 4.66	2.83 ± 0.13	13.01 ± 1.46	98.41 ± 2.67	3.07 ± 0.24
2	10.74 ± 1.01	97.28 ± 4.42	3.45 ± 0.15	12.93 ± 1.43	98.40 ± 2.79	3.67 ± 0.23
3	11.26 ± 0.96	97.52 ± 4.28	4.10 ± 0.19	12.90 ± 1.44	98.40 ± 2.79	4.29 ± 0.25
4	11.91 ± 0.92	97.96 ± 3.53	4.72 ± 0.25	13.06 ± 1.51	98.56 ± 2.35	4.86 ± 0.31
5	12.65 ± 0.90	98.27 ± 2.91	5.21 ± 0.30	13.29 ± 1.56	98.60 ± 2.25	5.30 ± 0.35

TABLE V. Evaluation of combined pipelines on SCVP trained on the singleview dataset [6] and MA-SCVP trained on the long-tail multiview dataset: Each value is the mean value and its standard deviation, computed over 3,000 tests. **RV**, **VSC**, and **MC** stand for the number of required views, visible surface coverage, and movement cost, respectively. Note that $k = 0$ means the input of only the initial view (singleview-activated) while $k \geq 1$ means the input of the initial view and the additional k NBVs from **PCNBV** (multiview-activated). As can be seen, MA-SCVP achieves a consistently high VSC with only a single NBV ($k = 1$), exhibiting a stable plateau across $k = 1, 2, 3, 4, 5$ NBVs combined. This makes 1-NBV+MA-SCVP our final choice and t -tests shown in Table VI are analyzed to further confirm our choice.

NBV submodule, (2) the selected network for our one-shot submodule, and (3) the number k of NBVs combined.

1) *Determination of NBV Submodule*: Table IV reports the iterative reconstruction results of two NBV networks and four search methods in terms of VSC. From the results, we have two major findings:

- PCNBV outperforms the other methods achieving higher coverage in the early iterations (1-5).
- Learning-based methods exhibit inferior VSC compared to search-based methods in later iterations, highlighting challenges in high-quality *unknown* object reconstruction.

Based on these findings, we finally select the best-performing PCNBV as our NBV submodule because we only employ NBVs in the early iterations.

2) *Determination of One-Shot Submodule and Number k* :

Table V reports the final reconstruction results of our combined pipelines with $k = 0 - 5$ NBVs from PCNBV on both the SCVP network trained on the singleview dataset [6] and our MA-SCVP network trained on the long-tail multiview dataset. From the results, we have four major findings:

- Increasing the number k of NBVs incorporated into SCVP enhances VSC but simultaneously leads to an increase in RV and MC. This suggests that incorporating *online* surface information from NBV perception data enhances the performance of the one-shot network. However, training it solely on the singleview dataset renders it unsuitable for our pipeline as reflected in the increased RV and MC.
- Without incorporating NBVs ($k = 0$), MA-SCVP trained on the long-tail multiview dataset exhibits a significantly higher VSC compared to SCVP trained on the singleview dataset. This suggests that our long-tail multiview sampling and multiview-activated architecture *offline* provide more geometric knowledge to the network.
- When incorporating NBVs into MA-SCVP, a single NBV ($k = 1$) proves adequate to achieve a high VSC. Adding

Method	Reference Method	Significance		
		RV	VSC	MC
0-NBV+MA-SCVP	0-NBV+SCVP	TRUE	TRUE	TRUE
1-NBV+MA-SCVP	0-NBV+MA-SCVP	FALSE	TRUE	TRUE
2-NBV+MA-SCVP	1-NBV+MA-SCVP	FALSE	FALSE	TRUE
3-NBV+MA-SCVP	1-NBV+MA-SCVP	FALSE	FALSE	TRUE
4-NBV+MA-SCVP	1-NBV+MA-SCVP	FALSE	FALSE	TRUE
5-NBV+MA-SCVP	1-NBV+MA-SCVP	TRUE	FALSE	TRUE

TABLE VI. t -tests on different combined pipelines in Table V: Each value is whether the difference between two methods is significant or not according to the student t -test with a p -value of 0.001. **RV**, **VSC**, and **MC** stand for the number of required views, visible surface coverage, and movement cost, respectively. As can be seen, (1) 0-NBV+MA-SCVP exhibits a significant VSC increase compared to 0-NBV+SCVP, indicating the effectiveness of our long-tail multiview sampling; (2) 1-NBV+MA-SCVP exhibits a significant VSC increase compared to 0-NBV+MA-SCVP, indicating the effectiveness of our combined pipeline with a single NBV; (3) the rest k -NBV+MA-SCVP ($k = 2, 3, 4, 5$) do not exhibit a significant VSC increase compared to 1-NBV+MA-SCVP but require a significant higher MC. These confirm a single NBV is sufficient for our MA-SCVP to achieve both high-quality and high-efficiency reconstruction of unknown objects.

more NBVs ($k = 2, 3, 4, 5$) yields no significant benefit for VSC, as a stable plateau is observed. This trend is confirmed by the results of the t -tests on these pipelines presented in Table VI.

- Furthermore, incorporating more NBVs into MA-SCVP consistently results in a substantial increase in MC. For instance, achieving a non-significant VSC improvement would necessitate an additional 50% movement (comparing $k = 4$ to $k = 1$), which is not deemed worthwhile.

Based on these findings, we settle on the following choices: (1) PCNBV for the NBV submodule, (2) MA-SCVP for the one-shot submodule, and (3) opting for $k = 1$ as the number of NBV combined. Therefore, the following 1-NBV+MA-SCVP stands for this determined pipeline.

To offer a more thorough comprehension of our pipeline, we introduce an analysis of how different NBV submodules influence MA-SCVP performance in Appendix B-B.

System Type	Stop Criterion	Method	RV	VSC (%)	MC (m)
Iterative NBV	m -based ($< 0.5\%$)	PCNBV [8]	6.96 \pm 1.64	95.86 \pm 2.90	3.74 \pm 0.88
		NBVNet [10]	6.94 \pm 1.90	93.61 \pm 5.71	3.70 \pm 1.03
		RSE [7]	7.33 \pm 2.33	93.39 \pm 6.06	3.22 \pm 1.10
		APORA [48]	7.13 \pm 2.09	92.52 \pm 6.72	3.34 \pm 1.27
		MCMF [49]	7.06 \pm 1.88	95.34 \pm 4.33	3.54 \pm 1.07
		GMC [50]	7.06 \pm 1.84	95.59 \pm 3.83	3.54 \pm 1.04
		RSE+Mov [7]	7.13 \pm 2.38	90.66 \pm 7.50	2.70 \pm 1.11
		APORA+Mov [48]	7.13 \pm 2.06	92.49 \pm 6.71	3.30 \pm 1.23
		MCMF+Mov [49]	8.02 \pm 2.33	92.60 \pm 10.12	2.40 \pm 0.91
		GMC+Mov [50]	6.89 \pm 1.86	93.73 \pm 4.98	2.80 \pm 0.94
	m -based ($< 0.1\%$)	PCNBV [8]	10.40 \pm 3.30	97.07 \pm 2.33	5.21 \pm 1.36
		NBVNet [10]	10.37 \pm 3.55	95.62 \pm 4.67	5.35 \pm 1.64
		RSE [7]	11.74 \pm 3.99	97.32 \pm 2.87	4.62 \pm 1.46
		APORA [48]	11.76 \pm 3.92	96.44 \pm 4.43	5.52 \pm 1.96
		MCMF [49]	11.39 \pm 3.83	97.85 \pm 2.40	5.73 \pm 1.94
		GMC [50]	11.27 \pm 3.82	97.86 \pm 2.29	5.57 \pm 1.80
		RSE+Mov [7]	11.70 \pm 4.22	95.50 \pm 4.97	3.91 \pm 1.50
		APORA+Mov [48]	11.74 \pm 3.91	96.41 \pm 4.42	5.37 \pm 1.89
		MCMF+Mov [49]	12.47 \pm 3.79	97.46 \pm 4.65	4.15 \pm 1.46
		GMC+Mov [50]	11.46 \pm 4.18	96.80 \pm 3.60	4.28 \pm 1.62
One-Shot	Auto-Stop	SCVP [6]	9.61 \pm 0.96	96.12 \pm 6.29	2.28 \pm 0.15
Combined (Ours)	Auto-Stop	1-NBV+MASCVP	13.01 \pm 1.46	* 98.41 \pm 2.67	3.07 \pm 0.24

TABLE VII. Evaluation of three types of view planning systems: iterative NBV, one-shot, and combined. Each value is the mean value and its standard deviation, computed over 3,000 tests. m -based stop criterion [82], [83] finishes the reconstruction when the variation in the number of frontier voxels becomes smaller than a threshold for consecutive $m = 3$ sensing operations. The threshold is set to 0.1% (strict) or 0.5% (lenient) of the total voxels. **+Mov** stands for the movement-cost weighted NBV evaluation. **RV**, **VSC**, and **MC** stand for the number of required views, visible surface coverage, and movement cost, respectively. The star indicates significance according to the student t -test with a p -value of 0.001. As can be seen, our 1-NBV+MASCVP achieves a significantly higher VSC than all baselines, while reducing MC by 45% compared to the second-highest VSC method (GMC with $< 0.1\%$).

E. Reconstruction Study on System Performance

A typical view planning system needs two major setups: (1) the view planning method, and (2) the stop criterion.

1) *System Setup*: Our *combined* system utilizes the 1-NBV+MA-SCVP method with an auto-stop criterion.

For the *one-shot* system, the SCVP method [6] also contains an auto-stop criterion.

For *iterative* NBV systems, most view planning methods are designed to maximize surface coverage, *i.e.*, enhancing reconstruction quality. Delmerico *et al.* [7] propose a simple way to consider reconstruction efficiency simultaneously for search-based methods, using the movement-cost weighted NBV evaluation:

$$utility(v) = \frac{gain(v)}{\sum_V gain} - \frac{cost(v)}{\sum_V cost} \quad (13)$$

where $gain(v)$ is the information gain defined for the search and $cost(v)$ is the movement cost of a candidate view. This cost is defined in such a way that the farther away a candidate view is from the view position in the current iteration, the higher the cost value, resulting in a lower $utility(v)$ for that candidate view. We incorporate this weighting approach for search-based methods, with the exception of GMC [50], which has its own movement-cost weight. To distinguish them, we append the tag **+Mov** after the names of the search-based methods.

It is important to note that our auto-stop criterion is only achievable by running our network, which is not feasible for NBV methods. As demonstrated in the literature for NBV stopping tests [82], [83], the m -based stop criterion exhibits the highest reconstruction quality among different criteria. For unknown scenarios, this criterion finishes the reconstruction when the variation in the number of frontier voxels becomes smaller than a threshold for consecutive m sensing operations. A frontier voxel is an unknown voxel and has at least one free and one occupied neighbor. m is set to 3. We explore both a

Method	Inference Time (s)	Inference Number
RSE [7]	1.134 \pm 0.178	About 7 (lenient) or 11 (strict)
APORA [48]	1.141 \pm 0.175	
MCMF [49]	1.274 \pm 0.312	
GMC [50]	1.518 \pm 1.155	
PCNBV [8]	0.099 \pm 0.019	
NBVNet [10]	0.006 \pm 0.001	
SCVP [6]	0.112 \pm 0.121	
1-NBV+MASCVP (Ours)	0.119 \pm 0.038	2

TABLE VIII. Evaluation of inference time of different methods: The mean time for inferring view planning module once and its standard deviation are reported, computed over 3,000 tests. The number of inferences for NBV methods depends on the stop criterion, which is approximately 7 or 11. As can be seen, learning-based methods are much faster than search-based methods.

strict and lenient threshold, computed based on the number of voxels representing 0.1% and 0.5% of the total within the $32 \times 32 \times 32$ object bounding box, respectively.

2) *Comparison of System Performance*: Table VII reports the comparison of different types of view planning systems. Note that the results of PCNBV and NBVNet trained on the NBVR dataset are reported here, as they demonstrate better performance in the later iterations. From the results, we have four major findings:

- With a lenient stop criterion, iterative NBV systems achieve a comparable MC against our combined system but exhibit much lower VSC.
- With a strict stop criterion, iterative NBV systems achieve a comparable VSC against our combined system but exhibit much higher MC.
- Our combined system achieves a significant improvement in VSC compared to all iterative NBV systems and the one-shot system.
- Our combined system reduces MC by 45% compared to the second-highest VSC method (GMC with $< 0.1\%$).

Besides, the results also validate that our system provides an effective stop criterion. We further analyze it in Appendix B-C.

3) *Inference and Update Time*: Table VIII reports the time required for inferring view planning once using different meth-

ods. As a learning-based method, our system achieves a short inference time. Another factor influencing the reconstruction time is the OctoMap update time, which is measured at 0.163 ± 0.111 seconds for a single update. OctoMap-based NBV methods need to be updated at each iteration (about 7 or 11 in total), while our system requires only two updates (one for the initial view and one for NBV). This also indicates that the remaining number of required views does not reduce the efficiency of our system. Overall, our system exhibits high computational efficiency, totaling around 0.564 seconds.

Based on all these comparisons, we now conclude that our system achieves both high-quality and high-efficiency reconstruction of unknown objects.

F. Real-World Experiments

The hardware of our real-world system is a 6-DOF UR5 arm with an Intel Realsense D435 camera mounted on its end-effector. Experiments are performed on the ROS platform [84]. The physical constraints of the joints in our robot arm limit the workspace and movement. Some candidate view positions may be unreachable due to these constraints. To address this, we adjust the candidate view positions by moving them up by 0.008 m to ensure reachability. Additionally, the computed cartesian trajectories occasionally fail to follow our planned paths. To mitigate this, we lower the object center to the table height, allowing for less constrained view poses. This adjustment has minimal impact on the reconstruction since the object remains within the camera field of view. If these adjustments still result in path failures, we directly solve the joint inverse solution for the target view. Importantly, these adjustments are consistent across all methods, ensuring a valid and fair comparison.

1) *Ground Truth Model and Noise*: To calculate the surface coverage, having a ground truth model of the object is essential. This is achieved by collecting point clouds from the entire view space and voxelizing them to 0.002 m, serving as the ground truth model. It is worth mentioning that slight calibration errors may result in a small offset in the point cloud for each view. To address this issue, for a voxel on the ground truth model, we search for its corresponding neighbors. If any neighboring voxels are covered, it is included in the coverage count. However, achieving 100% surface coverage in a real reconstruction trail is challenging due to sensor noise in the real world. Factors such as lighting and environmental conditions can affect the accuracy of depth camera perception, introducing some noise points. Fig. 14 illustrates real-world noise. While noise points are inevitable (less than 1%), the comparison remains valid and fair as all methods utilize the same camera configuration.

2) *Dynamic Object Bounding Box and View Space*: The object center and size are known in advance in simulation, *i.e.*, the object bounding box with an edge length equal to two times the size is determined. However, in the real world, this information is unknown. Therefore, we employ a dynamic strategy to obtain the bounding box of an object. As shown in Fig. 15, the bounding box is dynamically updated based on the partially reconstructed point clouds of the object. Therefore, the center of the view space undergoes a corresponding change

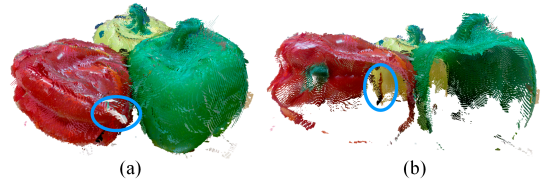


Fig. 14: An example illustrating real-world noise in the ground truth point cloud: (a) Outside perspective. (b) Inside perspective (cross-section). The areas marked in blue highlight some of the noise spots on the surface and noise inside the object.

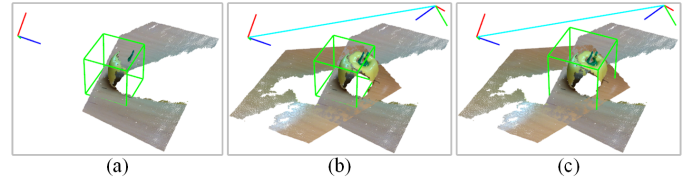


Fig. 15: Dynamic computation of the object center and size: partially reconstructed scenes, paths (cyan), planned views (red-green-blue), and the bounding box (green cube). (a) The bounding box is computed from the initial view. (b) Upon the arrival of the point cloud from the second view, it becomes evident that the existing bounding box is insufficient to encompass the entire object. (c) Subsequently, the bounding box is updated based on the new point cloud.

Method	RV	VSC (%)	MC (m)	RT (s)
Ours with GT	12.78 ± 1.09	99.36 ± 0.32	1.71 ± 0.19	102.5 ± 14.8
Ours Dynamic	12.93 ± 1.27	99.35 ± 0.29	1.73 ± 0.22	105.3 ± 12.6

TABLE IX. Evaluation of real-world generalization performance for unknown object center and size: **Ours with GT** denotes reconstruction based on the ground truth object center and size, whereas **Ours Dynamic** denotes reconstruction with dynamically updated object center and size. Each value is the mean value and its standard deviation, computed over 60 tests. **RV**, **VSC**, **MC**, and **RT** stand for the number of required views, visible surface coverage, movement cost, and reconstruction time, respectively. As can be seen, our system is not sensitive to deviations in the object center and size.

along with the object center as discussed in Sec. III-C. The sphere radius of the view space is set to the computed o_{size} plus 0.15 m because the camera needs a certain distance to obtain correct depth images.

3) *Object Test Cases*: We test three objects under different sizes: a single crop measuring 0.056 m (Fig. 15), cluttered crops measuring 0.093 m (Fig. 14), and a complex cup measuring 0.060 m (Fig. 16). We randomly assign two different object rotations, five initial views, and two repetitions for each object. In total, we conduct $3 \times 2 \times 5 \times 2 = 60$ test cases to mitigate the influence of potential noise.

4) *Generalization Study on Our System*: Since we need to employ the dynamic strategy in real-world scenarios, we investigate the sensitivity of our system to deviations in the object center and size. Table IX reports the results with and without ground truth. From the results, we confirm that (1) our system exhibits robust generalization capability to unknown object centers and sizes, and (2) our networks, trained solely in simulation, demonstrate satisfactory performance when directly deployed in a real-world environment.

5) *Comparison of System Performance*: Based on the results presented in Table VII, we select three baselines for comparison: the one-shot system SCVP and two iterative NBV systems of the best-performing GMC among NBV methods without movement weights and the best-performing MCMF+Mov among NBV methods with movement weights. For NBV systems, the stop criterion utilized is the m -based

Method	RV	VSC (%)	MC (m)	RT (s)
GMC [50]	12.22 ± 2.63	98.57 ± 1.36	2.92 ± 0.87	143.1 ± 31.7
MCMF+Mov [49]	12.77 ± 2.36	97.02 ± 3.04	1.44 ± 0.42	102.4 ± 18.9
SCVP [6]	10.2 ± 0.95	95.88 ± 4.28	1.28 ± 0.15	82.2 ± 11.7
Ours	12.93 ± 1.27	*99.35 ± 0.29	1.73 ± 0.22	105.3 ± 12.6

TABLE X. Evaluation of view planning systems with the dynamic strategy in the real world: GMC and MCMF+Mov adopt the m -based stop criterion ($m = 3$) with a threshold 0.4%. Each value is the mean value and its standard deviation, computed over 60 tests. **RV**, **VSC**, **MC**, and **RT** stand for the number of required views, visible surface coverage, movement cost, and reconstruction time, respectively. The star indicates significance according to the student t -test with a p -value of 0.001. As can be seen, our system achieves a significantly higher VSC than baselines, while also exhibiting substantial reductions in MC compared to the second-highest VSC method (GMC).

Method	VSC (%)	MC (m)	RT (s)
GMC [50]	98.97 ± 0.60	3.12 ± 0.70	150.0 ± 23.5
MCMF+Mov [49]	97.52 ± 1.85	1.45 ± 0.36	104.2 ± 15.3
Ours	*99.35 ± 0.29	1.73 ± 0.22	105.3 ± 12.6

TABLE XI. Evaluation of applying our stop criterion to NBV systems in the real world: Each value is the mean value and its standard deviation, computed over 60 tests. RV (the number of required views) of NBV systems is 12.93 ± 1.27 , which is the same as our system. **VSC**, **MC**, and **RT** stand for visible surface coverage, movement cost, and reconstruction time, respectively. The star indicates significance according to the student t -test with a p -value of 0.001. As can be seen, while our stop criterion markedly enhances NBV systems by increasing VSC and reducing standard deviation, our system still achieves a significantly higher VSC.

criterion ($m = 3$) with a threshold of 0.4% instead of 0.1% to achieve a similar performance as in the simulation. Note that all these systems are employed with the dynamic strategy. Table X presents the comparison to the three baselines. The results confirm that our system achieves both high-quality and efficient reconstruction of unknown objects in the real world.

6) *Stop Criterion Analysis*: In the case of NBV systems, adjusting the threshold of the stop criterion might require intervention from a human expert in the real world. Otherwise, it could stop prematurely or fail to stop altogether. In contrast, our system provides an auto-stop criterion that proves to be both sufficient and stable, as demonstrated in Table XI.

G. Object Test Case Complexity Analysis

To gain insight into how the provision of extra information enhances reconstruction quality, we analyze our systems in terms of object test case complexity. The complexity of a given object test case is influenced by several factors, including size, rotation, the difficulty of the initial view, and surface complexity. To quantify the complexity of a specific object test case, we employ the SCOP solution, as defined in Sec. IV-B. The resulting number of covering views from SCOP serves as an indicator of complexity. This is intuitive, since the more complex the situation, the more views are required to cover the remaining object surfaces. Table XII presents an analysis of object test case complexity within our systems in simulation. From the results, we confirm that (1) the offline training on our long-tail multiview dataset enhances overall performance (when comparing 0-NBV+MA-SCVP to SCVP); and (2) the online incorporation of a single NBV improves performance, particularly in more complex cases (when comparing 1-NBV+MA-SCVP to 0-NBV+MA-SCVP).

To validate this finding beyond simulation, we conduct a comparison in the real world using a complex cup. This cup features continuous surfaces with large variations in curvature, requiring top views to observe the middle surfaces. As shown

Number of Covering Views (Number of Test Cases)	4-7 (314)	8-12 (1729)	13-16 (957)
0-NBV+SCVP [6]	99.67 ± 0.41	97.85 ± 2.75	91.83 ± 9.08
0-NBV+MA-SCVP	99.95 ± 0.11	98.99 ± 1.73	95.87 ± 5.55
1-NBV+MA-SCVP (Ours)	99.95 ± 0.14	99.01 ± 1.48	96.84 ± 3.80
2-NBV+MA-SCVP	99.96 ± 0.06	98.99 ± 1.56	96.83 ± 4.02

TABLE XII. Evaluation of object test case complexity in simulation involves grouping the number of covering views into three categories: simple (4-7), medium (8-12), and complex (13-16). Each value is the mean VSC value with its standard deviation, computed over the number of test cases in its category. VSC stands for visible surface coverage. As can be seen, 1-NBV+MA-SCVP achieves the highest VSC in medium and complex cases, while maintaining a similar VSC in simple cases. This indicates that providing extra information to one-shot networks contributes to improved performance.

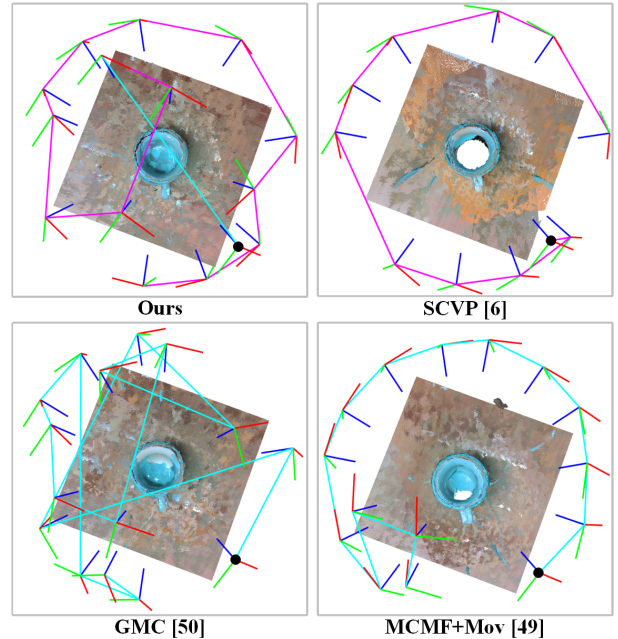


Fig. 16: Comparison of reconstruction process on a complex cup: reconstructed scenes and 3D models, local paths (cyan), global paths (purple), planned views (red-green-blue), and the same initial view (black circle). As can be seen, (1) SCVP fails to capture the missing middle surfaces, confirming the enhanced quality of complex cases in our system; and (2) our system reconstructed more surfaces (in comparison to MCMF+Mov) within shorter paths (in comparison to GMC).

in Fig. 16, our system successfully plans top views to observe the missing surfaces, in contrast to SCVP. The full comparative reconstruction processes are illustrated in our demo video.

VI. DISCUSSION

Although our system can achieve compelling results in experiments, there are still some important aspects left for future work. First, the VSC is only 96.84 ± 3.80 for those complex cases, as shown in Table XII. We observe that some objects in the simulation datasets have holes on their surfaces, *i.e.*, discontinuous surfaces. For instance, the Cheff object (the last one in the bottom-right corner in Fig. 12) has two holes on its surfaces. However, this type of complexity falls outside the scope of this paper since the majority of real-world objects are solid inside. Specifically, this complexity arises from the need for specific views to observe surfaces inside the object. Predicting these specific views might pose a challenge for convolutional networks, given that the assumption of continuous and watertight surfaces is common in surface feature extraction [85]. In particular, predicting the number and the

shape of holes in unknown areas is challenging without real perception. A possible solution is to detect these holes after the initial reconstruction using our system and then plan additional views to observe the inner surfaces along these holes.

Second, the candidate view space is pre-defined, and the network output is bound to a certain candidate view. This does not allow the system to drop some unreachable candidate views, such as due to obstacles and robot workspace. A possible solution is using a regression network [56] and training it with the state of unreachable views.

Third, we assume that there is only one object in the workspace. Therefore, reconstructing multiple objects or an object with multiple regions of interest requires manual separations. This might be improved by point-cloud segmentation methods [86] or the detection pipeline [87].

Fourth, although objects of any size can be reconstructed as long as the size does not exceed a maximum size bound, the system cannot handle larger objects such as chairs and large plants. A possible solution is to detect the object size in advance, which can be solved by some exploration methods [15].

Finally, the bottom surfaces of an object cannot be reconstructed on a tabletop. Although such a model is sufficient for many applications such as grasping and phenotyping, it is better to have a watertight and enclosed 3D model. There are some solutions to address the lack of bottom surfaces. Wu *et al.* [32] placed the object in the air with a stand. Krainin *et al.* [45] lifted the object with a robotic arm to scan the object from all directions. Another possible solution is to pick up and put down the object to observe the previous bottom surface.

VII. CONCLUSION

In this work, we present a novel combined system that integrates one-shot view planning with a single next-best view through long-tail multiview sampling. Our long-tail sampling method addresses unbalanced importance among multiview inputs, presenting an efficient training dataset. The trained MA-SCVP network provides effective view planning with an auto-stop criterion learned from the set covering. Facing unknown environments, we demonstrate that both offline and online providing extra information improves surface coverage, especially in complex object cases. As a result, our system achieves both high-quality and high-efficiency reconstruction compared to state-of-the-art view planning systems. Real-world experiments demonstrate the robust generalization and deployment of our system.

APPENDIX A

NBV RECONSTRUCTION AND SAMPLING SPACE

To generate the whole sampling space C_{whole} , we performed NBV reconstruction trails in the simulation as summarized in Algorithm 4. The reconstruction needs the object mesh model set O , rotation set R , and candidate view space V as input. It is worth mentioning that the candidate view space is pre-defined and our network output is bound to a certain candidate view. This implies the inputs to the network have lost the information of rotational invariance and symmetry in the hemispherical view space. Consequently, we incorporate R and V to enable the network to generalize across various object rotations and

Algorithm 4 NBV Reconstruction with Ground Truth

Require: Object Set O , Rotation Set R , View Space V

```

1: for all  $o \in O$  and  $r \in R$  do
2:    $c_{obj} \leftarrow (o, r)$ 
3:   for all  $v \in V$  do
4:      $\mathfrak{v} \leftarrow \text{VirtualImaging}(c_{obj}, v)$ 
5:      $U \leftarrow U \cup \mathfrak{v}$ 
6:   end for
7:   for all  $v \in V$  do
8:      $U_{cover} \leftarrow \mathfrak{v}$ 
9:      $c_{view} \leftarrow \text{BitInit}(v)$ 
10:     $C_{whole} \leftarrow C_{whole} \cup \{(c_{obj}, c_{view})\}$ 
11:     $VSC \leftarrow \frac{|U_{cover}|}{|U|}$ 
12:    while  $VSC \neq 100\%$  do
13:       $v^* \leftarrow \arg \max_v |\mathfrak{v} \setminus U_{cover}|$ 
14:       $U_{cover} \leftarrow U_{cover} \cup \mathfrak{v}^*$ 
15:       $n_{select} \leftarrow \text{PopCount}(c_{view})$ 
16:       $NS(c_{obj}, n_{select}) \leftarrow \text{Update with } \frac{|U_{cover}|}{|U|} - VSC$ 
17:       $c_{view} \leftarrow \text{BitUpdate}(v^*)$ 
18:       $C_{whole} \leftarrow C_{whole} \cup \{(c_{obj}, c_{view})\}$ 
19:       $VSC \leftarrow \frac{|U_{cover}|}{|U|}$ 
20:    end while
21:  end for
22: end for
23: return  $C_{whole}$ 

```

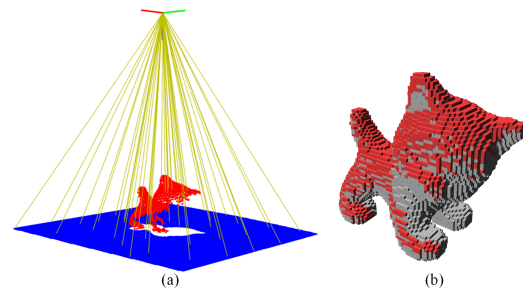


Fig. 17: Virtual imaging: (a) Some rays of a view v in point-cloud space (yellow). (b) The set \mathfrak{v} of object voxels (red) and uncovered voxels (gray) in the ground truth model.

initial views during the reconstruction process. An object case $c_{obj} = (o, r)$ is an object $o \in O$ from 3D model datasets (as described in Sec. V-A) with its rotation set $r \in R$ (line 2). The number $|O|$ of 3D models used for training is 40. We rotate the model around the $Z+$ (the vertically upward direction of the table) by a degree varying from 0° to 360° in steps of 45° , *i.e.*, the number $|R|$ of the rotation is 8. The total number of reconstruction trails is $40 \times 8 \times 32 = 10,240$.

Before the reconstruction trails, we perform virtual imaging for all candidate views on an object case c_{obj} (lines 3-6). The set \mathfrak{v} of object surface voxels that can be observed from a view $v \in V$ is obtained by virtual imaging (line 4). Since the bottom and inner voxels are completely invisible, we generate a universe set $U = \bigcup_{v \in V} \mathfrak{v}$ of all visible surface voxels as the ground truth (line 5). As shown in Fig. 17, virtual imaging in our simulated reconstruction is implemented with the ray-casting operation of OctoMap, which is common in voxel-based view planning [7]. We insert an object case into an OctoMap and get visible voxels in it from the cast rays of a

λ ($\gamma = 0.5$)	1.0	1.5	2.0	2.5	3.0
Recall (%)	62.18	67.49	83.95	86.45	86.71
Precision (%)	87.29	80.00	85.76	64.95	62.44
F_1 (%)	72.63	73.21	84.84	74.17	72.60
γ ($\lambda = 2.0$)	0.1	0.3	0.5	0.7	0.9
Recall (%)	100.00	99.71	83.95	69.76	39.57
Precision (%)	49.90	66.97	85.76	88.51	90.33
F_1 (%)	66.58	80.12	84.84	78.02	55.04

TABLE XIII. Ablation study on MA-SCVP parameters: Each value is computed on the validation set. As can be seen, $\lambda = 2.0$ and $\gamma = 0.5$ leads to the highest F_1 score.

1-NBV Submodule	First Iteration VSC (%)	RV	VSC (%)	MC (m)
PCNBV [8]	71.90 \pm 8.63	13.01 \pm 1.46	98.41 \pm 2.67	3.07 \pm 0.24
NBVNet [10]	71.01 \pm 9.12	12.95 \pm 1.46	98.32 \pm 2.84	3.06 \pm 0.23
RSE [7]	68.29 \pm 10.37	13.07 \pm 1.43	98.16 \pm 3.56	3.09 \pm 0.24
APORA [48]	64.67 \pm 9.34	13.63 \pm 1.39	98.38 \pm 3.23	3.08 \pm 0.21
MCMF [49]	64.12 \pm 10.09	13.20 \pm 1.47	98.31 \pm 3.19	3.01 \pm 0.25
GMC [50]	64.19 \pm 10.07	13.19 \pm 1.49	98.30 \pm 3.25	3.01 \pm 0.25
Random	58.23 \pm 10.84	13.41 \pm 1.45	98.22 \pm 3.48	2.93 \pm 0.26

TABLE XIV. Evaluation of different NBV submodules within our 1-NBV+MA-SCVP pipeline: Each value is the mean value and its standard deviation, computed over 3,000 tests. **RV**, **VSC**, and **MC** stand for the number of required views, visible surface coverage, and movement cost, respectively. As can be seen, since PCNBV achieves the highest VSC of the first NBV iteration, our 1-NBV+MA-SCVP pipeline achieves the highest VSC and lowest standard deviation when PCNBV is used as the NBV submodule.

given view. A ray is cast by the de-projecting pixels of the virtual image plane until it hits an occupied voxel. The object model is converted into a dense point cloud before insertion into the OctoMap to ensure that the object surface is closed.

A reconstruction trail starts with an initial view from the candidate view space (lines 8-11). U_{cover} stands for the current number of covered object voxels (lines 8 and 14), c_{view} is initialized and updated by the view bit (lines 9 and 17), and VSC stands for current visible surface coverage (lines 11 and 19). The NBV can be easily determined from the view that observes the most uncovered surface voxels in the ground truth (line 13). $PopCount$ calculates the number of 1 bit, *i.e.*, the number of visited views (line 15). NS is a hash table that maps the paired object case and the number n_{select} of selected views to the total averaged surface coverage gain. $Update$ will replace the old average value with the new one calculated from the current surface coverage gain $|U_{cover}|/|U| - VSC$ (line 16). The input cases for each iteration are stored to generate the whole sampling space C_{whole} (lines 10 and 18). Traditional sampling methods [8], [10] can be regarded as modifying $v \in V$ in line 7 to $v \in V_{ran}$, where V_{ran} is a random subset of V .

APPENDIX B

SUPPLEMENTARY SIMULATION EXPERIMENTS

A. Ablation Study on MA-SCVP Parameters

We determine the MA-SCVP parameter values based on the highest F_1 score, following the strategy outlined in SCVP [6]. Table XIII reports the ablation study. The results indicate that $\lambda = 2.0$ and $\gamma = 0.5$ are valid for the MA-SCVP network.

B. NBV Submodule Analysis

As discussed in Sec. III-B, our system allows for integration with various NBV methods. To examine the correlation between NBV method performance and our MA-SCVP network, we replace PCNBV with alternative NBV methods, including a random method, in our 1-NBV+MA-SCVP pipeline. Table XIV reports the results of different NBV submodules. From the results, we confirm that (1) VSC increases when any NBV method is applied in our 1-NBV+MA-SCVP pipeline,

Method	VSC (%)	MC (m)
PCNBV [8]	97.51 \pm 2.09	6.14 \pm 1.03
NBVNet [10]	96.79 \pm 4.02	6.68 \pm 1.15
RSE [7]	97.89 \pm 1.88	4.92 \pm 0.84
APORA [48]	98.00 \pm 2.00	6.12 \pm 1.00
MCMF [49]	98.70 \pm 1.27	6.57 \pm 0.97
GMC [50]	98.65 \pm 1.21	6.42 \pm 0.93
RSE+Mov [7]	97.06 \pm 2.67	4.22 \pm 0.87
APORA+Mov [48]	97.96 \pm 2.01	5.95 \pm 0.95
MCMF+Mov [49]	98.42 \pm 1.58	4.43 \pm 0.93
GMC+Mov [50]	98.26 \pm 1.50	4.85 \pm 0.94
1-NBV+MASCVP (Ours)	98.41 \pm 2.67	3.07 \pm 0.24

TABLE XV. Evaluation of applying our stop criterion to different NBV methods: Each value is the mean value and its standard deviation, computed over 3,000 tests. RV (the number of required views) of all methods is 13.01 \pm 1.46, which is the same as our system. **VSC**, and **MC** stand for the number of required views, visible surface coverage, and movement cost, respectively. As can be seen, our stop criterion enhances the VSC for all NBV methods but also demands a much higher MC.

Method	RV	VSC (%)	MC (m)
Random with Global Path Planning	12	95.96 \pm 3.11	2.64 \pm 0.18
	13	96.55 \pm 2.76	2.79 \pm 0.17
	14	97.02 \pm 2.47	2.94 \pm 0.16
	15	97.42 \pm 2.20	3.08 \pm 0.15
	16	97.77 \pm 1.98	3.22 \pm 0.15
	13.01 \pm 1.46	96.42 \pm 3.00	2.79 \pm 0.28
1-NBV+MASCVP (Ours)	13.01 \pm 1.46	* 98.41 \pm 2.67	3.07 \pm 0.24

TABLE XVI. Evaluation of random methods with a fixed number of views and our stop criterion: Each value is the mean value and its standard deviation, computed over 3,000 tests. **RV**, **VSC**, and **MC** stand for the number of required views, visible surface coverage, and movement cost, respectively. The star indicates significance according to the student t -test with a p -value of 0.001. As can be seen, our 1-NBV+MASCVP achieves a significantly higher VSC against random methods, indicating our effective stop criterion.

compared to 0-NBV+MA-SCVP (98.10 \pm 3.73); and (2) there is a generally positive correlation between the performance of the NBV method and the performance of our MA-SCVP network, *i.e.*, the higher the performance of the NBV method, the higher the performance of our MA-SCVP network (higher VSC with lower standard deviation).

C. Stop Criterion Analysis

To further validate that our 1-NBV+MA-SCVP provides an efficient stop criterion, we conduct two additional experiments. First, we allow NBV baselines to run until they reach the same number of views as our system. Table XV reports the results of applying our stop criterion to different NBV methods. From the results, we observe that (1) our stop criterion provides a sufficient number of required views; (2) MCMF+Mov achieves a similar VSC as ours but requires 40% more MC, highlighting the efficiency of our system; and (3) MCMF and GMC achieve a slightly higher VSC as ours but demand 110% more MC, which is not worthwhile.

Second, we randomly select a fixed number of views and utilize our global path planning for comparison. The fixed number of views is determined by prior knowledge regarding how many NBVs are required to fully cover an object, specifically 12-16, as shown in Fig. 6. It is important to note that these values are derived from training objects, and acquiring this knowledge in advance for unknown objects in real testing is unrealistic. Table XVI reports the results of random methods. From the results, we observe that (1) random methods require more RV and MC to achieve a comparable VSC than our method; and (2) the random method with our stop criterion confirms that our method not only predicts a sufficient RV but also effectively anticipates the view configuration, *i.e.*, which candidate views are needed to be selected.

REFERENCES

- [1] T. Zaenker, C. Smitt, C. McCool, and M. Bennewitz, "Viewpoint planning for fruit size and position estimation," in *2021 IEEE/RSJ International Conference on Intelligent Robots and Systems (IROS)*. IEEE, 2021, pp. 3271–3277.
- [2] N. Dengler, S. Pan, V. Kalagaturu, R. Menon, M. Dawood, and M. Bennewitz, "Viewpoint push planning for mapping of unknown confined spaces," *2023 IEEE/RSJ International Conference on Intelligent Robots and Systems (IROS)*, 2023.
- [3] M. Breyer, L. Ott, R. Siegart, and J. J. Chung, "Closed-loop next-best-view planning for target-driven grasping," in *2022 IEEE/RSJ International Conference on Intelligent Robots and Systems (IROS)*. IEEE, 2022, pp. 1411–1416.
- [4] S. Chen, Y. Li, and N. M. Kwok, "Active vision in robotic systems: A survey of recent developments," *The International Journal of Robotics Research*, vol. 30, no. 11, pp. 1343–1377, 2011.
- [5] R. Zeng, Y. Wen, W. Zhao, and Y.-J. Liu, "View planning in robot active vision: A survey of systems, algorithms, and applications," *Computational Visual Media*, pp. 1–21, 2020.
- [6] S. Pan, H. Hu, and H. Wei, "Scvp: Learning one-shot view planning via set covering for unknown object reconstruction," *IEEE Robotics and Automation Letters*, vol. 7, no. 2, pp. 1463–1470, 2022.
- [7] J. Delmerico, S. Isler, R. Sabzevari, and D. Scaramuzza, "A comparison of volumetric information gain metrics for active 3d object reconstruction," *Autonomous Robots*, vol. 42, no. 2, pp. 197–208, 2018.
- [8] R. Zeng, W. Zhao, and Y.-J. Liu, "Pc-nbv: A point cloud based deep network for efficient next best view planning," in *2020 IEEE/RSJ International Conference on Intelligent Robots and Systems (IROS)*. Las Vegas, NV, USA: IEEE, 2020, pp. 7050–7057.
- [9] Y. Zhang, B. Kang, B. Hooi, S. Yan, and J. Feng, "Deep long-tailed learning: A survey," *arXiv preprint arXiv:2110.04596*, 2021.
- [10] M. Mendoza, J. I. Vasquez-Gomez, H. Taud, L. E. Sucar, and C. Reta, "Supervised learning of the next-best-view for 3d object reconstruction," *Pattern Recognition Letters*, vol. 133, pp. 224–231, 2020.
- [11] C. Connolly, "The determination of next best views," in *1985 IEEE international conference on robotics and automation*, vol. 2. St. Louis, MO, USA: IEEE, 1985, pp. 432–435.
- [12] K. A. Tarabanis, P. K. Allen, and R. Y. Tsai, "A survey of sensor planning in computer vision," *IEEE transactions on Robotics and Automation*, vol. 11, no. 1, pp. 86–104, 1995.
- [13] W. R. Scott, G. Roth, and J.-F. Rivest, "View planning for automated three-dimensional object reconstruction and inspection," *ACM Computing Surveys (CSUR)*, vol. 35, no. 1, pp. 64–96, 2003.
- [14] M. Maboudi, M. Homaei, S. Song, S. Malihi, M. Saadatseresht, and M. Gerke, "A review on viewpoints and path planning for uav-based 3d reconstruction," *IEEE Journal of Selected Topics in Applied Earth Observations and Remote Sensing*, 2023.
- [15] A. Bircher, M. Kamel, K. Alexis, H. Oleynikova, and R. Siegart, "Receding horizon path planning for 3d exploration and surface inspection," *Autonomous Robots*, vol. 42, pp. 291–306, 2018.
- [16] R. Monica, J. Aleotti, and D. Piccinini, "Humanoid robot next best view planning under occlusions using body movement primitives," in *2019 IEEE/RSJ International Conference on Intelligent Robots and Systems (IROS)*. IEEE, 2019, pp. 2493–2500.
- [17] S. Song, D. Kim, and S. Jo, "Online coverage and inspection planning for 3d modeling," *Autonomous Robots*, vol. 44, no. 8, pp. 1431–1450, 2020.
- [18] S. Song, D. Kim, and S. Choi, "View path planning via online multiview stereo for 3-d modeling of large-scale structures," *IEEE Transactions on Robotics*, 2021.
- [19] J. I. Vasquez-Gomez, L. E. Sucar, and R. Murrieta-Cid, "Hierarchical ray tracing for fast volumetric next-best-view planning," in *2013 International Conference on Computer and Robot Vision*. Regina, CANADA: IEEE, 2013, pp. 181–187.
- [20] J. Aleotti, D. L. Rizzini, R. Monica, and S. Caselli, "Global registration of mid-range 3d observations and short range next best views," in *2014 IEEE/RSJ International Conference on Intelligent Robots and Systems*. IEEE, 2014, pp. 3668–3675.
- [21] R. Monica and J. Aleotti, "Contour-based next-best view planning from point cloud segmentation of unknown objects," *Autonomous Robots*, vol. 42, pp. 443–458, 2018.
- [22] W. Peng, Y. Wang, Z. Miao, M. Feng, and Y. Tang, "Viewpoints planning for active 3-d reconstruction of profiled blades using estimated occupancy probabilities (eop)," *IEEE Transactions on Industrial Electronics*, vol. 68, no. 5, pp. 4109–4119, 2020.
- [23] A. K. Burusa, E. J. van Henten, and G. Kootstra, "Attention-driven active vision for efficient reconstruction of plants and targeted plant parts," *arXiv preprint arXiv:2206.10274*, 2022.
- [24] L. M. Wong, C. Dumont, and M. A. Abidi, "Next best view system in a 3d object modeling task," in *Proceedings 1999 IEEE International Symposium on Computational Intelligence in Robotics and Automation. CIRA'99 (Cat. No. 99EX375)*. IEEE, 1999, pp. 306–311.
- [25] T. Zaenker, C. Lehnert, C. McCool, and M. Bennewitz, "Combining local and global viewpoint planning for fruit coverage," in *2021 European Conference on Mobile Robots (ECMR)*. IEEE, 2021, pp. 1–7.
- [26] C. Wu, R. Zeng, J. Pan, C. C. Wang, and Y.-J. Liu, "Plant phenotyping by deep-learning-based planner for multi-robots," *IEEE Robotics and Automation Letters*, vol. 4, no. 4, pp. 3113–3120, 2019.
- [27] M. Lauri, J. Pajarinen, J. Peters, and S. Frintrap, "Multi-sensor next-best-view planning as matroid-constrained submodular maximization," *IEEE Robotics and Automation Letters*, vol. 5, no. 4, pp. 5323–5330, 2020.
- [28] L. Keselman, J. Iselin Woodfill, A. Grunnet-Jepsen, and A. Bhowmik, "Intel realsense stereoscopic depth cameras," in *Proceedings of the IEEE conference on computer vision and pattern recognition workshops*, 2017, pp. 1–10.
- [29] R. Border, J. D. Gammell, and P. Newman, "Surface edge explorer (see): Planning next best views directly from 3d observations," in *2018 IEEE International Conference on Robotics and Automation (ICRA)*. IEEE, 2018, pp. 6116–6123.
- [30] Z. Wu, S. Song, A. Khosla, F. Yu, L. Zhang, X. Tang, and J. Xiao, "3d shapenets: A deep representation for volumetric shapes," in *Proceedings of the IEEE conference on computer vision and pattern recognition*, 2015, pp. 1912–1920.
- [31] R. Pito, "A solution to the next best view problem for automated surface acquisition," *IEEE Transactions on pattern analysis and machine intelligence*, vol. 21, no. 10, pp. 1016–1030, 1999.
- [32] S. Wu, W. Sun, P. Long, H. Huang, D. Cohen-Or, M. Gong, O. Deussen, and B. Chen, "Quality-driven poisson-guided autoscanning," *ACM Transactions on Graphics*, vol. 33, no. 6, 2014.
- [33] A. Hornung, K. M. Wurm, M. Bennewitz, C. Stachniss, and W. Burgard, "Octomap: An efficient probabilistic 3d mapping framework based on octrees," *Autonomous robots*, vol. 34, no. 3, pp. 189–206, 2013.
- [34] N. A. Massios, R. B. Fisher *et al.*, *A best next view selection algorithm incorporating a quality criterion*. Citeseer, 1998, vol. 2.
- [35] R. Menon, T. Zaenker, and M. Bennewitz, "Nbv-sc: Next best view planning based on shape completion for fruit mapping and reconstruction," *2023 IEEE/RSJ International Conference on Intelligent Robots and Systems (IROS)*, 2023.
- [36] R. Monica and J. Aleotti, "Surfel-based next best view planning," *IEEE Robotics and Automation Letters*, vol. 3, no. 4, pp. 3324–3331, 2018.
- [37] B. Mildenhall, P. P. Srinivasan, M. Tancik, J. T. Barron, R. Ramamoorthi, and R. Ng, "Nerf: Representing scenes as neural radiance fields for view synthesis," *Communications of the ACM*, vol. 65, no. 1, pp. 99–106, 2021.
- [38] X. Pan, Z. Lai, S. Song, and G. Huang, "Activenerf: Learning where to see with uncertainty estimation," in *European Conference on Computer Vision*. Springer, 2022, pp. 230–246.
- [39] Y. Ran, J. Zeng, S. He, J. Chen, L. Li, Y. Chen, G. Lee, and Q. Ye, "Nurar: Neural uncertainty for autonomous 3d reconstruction with implicit neural representations," *IEEE Robotics and Automation Letters*, 2023.
- [40] L. Jin, X. Chen, J. Rückin, and M. Popović, "Neu-nbv: Next best view planning using uncertainty estimation in image-based neural rendering," in *2023 IEEE/RSJ International Conference on Intelligent Robots and Systems (IROS)*, 2023.
- [41] R. Border and J. D. Gammell, "Proactive estimation of occlusions and scene coverage for planning next best views in an unstructured representation," in *2020 IEEE/RSJ International Conference on Intelligent Robots and Systems (IROS)*. IEEE, 2020, pp. 4219–4226.
- [42] R. Border, Rowan and Gammell, Jonathan D, "The surface edge explorer (see): A measurement-direct approach to next best view planning," *arXiv preprint arXiv:2207.13684*, 2022.
- [43] S. Kriegel, T. Bodenmüller, M. Suppa, and G. Hirzinger, "A surface-based next-best-view approach for automated 3d model completion of unknown objects," in *2011 IEEE International Conference on Robotics and Automation*. IEEE, 2011, pp. 4869–4874.
- [44] I. D. Lee, J. H. Seo, Y. M. Kim, J. Choi, S. Han, and B. Yoo, "Automatic pose generation for robotic 3-d scanning of mechanical parts," *IEEE Transactions on Robotics*, vol. 36, no. 4, pp. 1219–1238, 2020.
- [45] M. Krainin, B. Curless, and D. Fox, "Autonomous generation of complete 3d object models using next best view manipulation planning,"

- in *2011 IEEE International Conference on Robotics and Automation*. Shanghai, PEOPLES R CHINA: IEEE, 2011, pp. 5031–5037.
- [46] J. I. Vasquez-Gomez, L. E. Sucar, R. Murrieta-Cid, and E. Lopez-Damian, “Volumetric next-best-view planning for 3d object reconstruction with positioning error,” *International Journal of Advanced Robotic Systems*, vol. 11, no. 10, p. 159, 2014.
- [47] J. I. Vasquez-Gomez, L. E. Sucar, and R. Murrieta-Cid, “View/state planning for three-dimensional object reconstruction under uncertainty,” *Autonomous Robots*, vol. 41, no. 1, pp. 89–109, 2017.
- [48] J. Daudelin and M. Campbell, “An adaptable, probabilistic, next-best view algorithm for reconstruction of unknown 3-d objects,” *IEEE Robotics and Automation Letters*, vol. 2, no. 3, pp. 1540–1547, 2017.
- [49] S. Pan and H. Wei, “A global max-flow-based multi-resolution next-best-view method for reconstruction of 3d unknown objects,” *IEEE Robotics and Automation Letters*, vol. 7, no. 2, pp. 714–721, 2022.
- [50] S. Pan and H. Wei, “A global generalized maximum coverage-based solution to the non-model-based view planning problem for object reconstruction,” *Computer Vision and Image Understanding*, vol. 226, p. 103585, 2023.
- [51] S. Lee, L. Chen, J. Wang, A. Liniger, S. Kumar, and F. Yu, “Uncertainty guided policy for active robotic 3d reconstruction using neural radiance fields,” *IEEE Robotics and Automation Letters*, vol. 7, no. 4, pp. 12 070–12 077, 2022.
- [52] N. Sünderhauf, J. Abou-Chakra, and D. Miller, “Density-aware nerf ensembles: Quantifying predictive uncertainty in neural radiance fields,” in *2023 IEEE International Conference on Robotics and Automation (ICRA)*. IEEE, 2023, pp. 9370–9376.
- [53] D. Peralta, J. Casimiro, A. M. Nilles, J. A. Aguilar, R. Atienza, and R. Cajote, “Next-best view policy for 3d reconstruction,” in *2020 European Conference on Computer Vision*. Glasgow, UK: Springer, 2020, pp. 558–573.
- [54] X. Zeng, T. Zaenker, and M. Bennewitz, “Deep reinforcement learning for next-best-view planning in agricultural applications,” in *2022 International Conference on Robotics and Automation (ICRA)*. IEEE, 2022, pp. 2323–2329.
- [55] Y. Zhou and O. Tuzel, “Voxelnet: End-to-end learning for point cloud based 3d object detection,” in *Proceedings of the IEEE conference on computer vision and pattern recognition*, 2018, pp. 4490–4499.
- [56] J. I. Vasquez-Gomez, D. Troncoso, I. Becerra, E. Sucar, and R. Murrieta-Cid, “Next-best-view regression using a 3d convolutional neural network,” *Machine Vision and Applications*, vol. 32, no. 2, pp. 1–14, 2021.
- [57] C. R. Qi, H. Su, K. Mo, and L. J. Guibas, “Pointnet: Deep learning on point sets for 3d classification and segmentation,” in *Proceedings of the IEEE conference on computer vision and pattern recognition*, 2017, pp. 652–660.
- [58] Y. Han, I. H. Zhan, W. Zhao, and Y.-J. Liu, “A double branch next-best-view network and novel robot system for active object reconstruction,” in *2022 International Conference on Robotics and Automation (ICRA)*. IEEE, 2022, pp. 7306–7312.
- [59] R. Monica and J. Aleotti, “A probabilistic next best view planner for depth cameras based on deep learning,” *IEEE Robotics and Automation Letters*, vol. 6, no. 2, pp. 3529–3536, 2021.
- [60] M. Peuzin-Jubert, A. Polette, D. Nozais, J.-L. Mari, and J.-P. Pernot, “Survey on the view planning problem for reverse engineering and automated control applications,” *Computer-Aided Design*, vol. 141, p. 103094, 2021.
- [61] M. D. Kaba, M. G. Uzunbas, and S. N. Lim, “A reinforcement learning approach to the view planning problem,” in *2017 IEEE Conference on Computer Vision and Pattern Recognition (CVPR)*. Honolulu, HI, USA: IEEE, 2017, pp. 5094–5102.
- [62] B. Hepp, M. Nießner, and O. Hilliges, “Plan3d: Viewpoint and trajectory optimization for aerial multi-view stereo reconstruction,” *ACM Transactions on Graphics (TOG)*, vol. 38, no. 1, pp. 1–17, 2018.
- [63] W. Jing, C. F. Goh, M. Rajaraman, F. Gao, S. Park, Y. Liu, and K. Shimada, “A computational framework for automatic online path generation of robotic inspection tasks via coverage planning and reinforcement learning,” *IEEE Access*, vol. 6, pp. 54 854–54 864, 2018.
- [64] V. Patidar and R. Tiwari, “Survey of robotic arm and parameters,” in *2016 International conference on computer communication and informatics (ICCCI)*. IEEE, 2016, pp. 1–6.
- [65] S. Chitta, “Moveit!: an introduction,” *Robot Operating System (ROS) The Complete Reference (Volume 1)*, pp. 3–27, 2016.
- [66] I. Enebuse, M. Foo, B. K. K. Ibrahim, H. Ahmed, F. Supmak, and O. S. Eyobu, “A comparative review of hand-eye calibration techniques for vision guided robots,” *IEEE Access*, 2021.
- [67] X.-F. Han, J. S. Jin, M.-J. Wang, W. Jiang, L. Gao, and L. Xiao, “A review of algorithms for filtering the 3d point cloud,” *Signal Processing: Image Communication*, vol. 57, pp. 103–112, 2017.
- [68] J. H. Conway and N. J. A. Sloane, *Sphere packings, lattices and groups*. Springer Science & Business Media, 2013, vol. 290.
- [69] M. Held and R. M. Karp, “A dynamic programming approach to sequencing problems,” *Journal of the Society for Industrial and Applied mathematics*, vol. 10, no. 1, pp. 196–210, 1962.
- [70] V. V. Vazirani, “Approximation algorithms (springer science & business media,” 2013.
- [71] H. Mittelmann, “Latest benchmark results,” in *Proceedings of the INFORMS Annual Conference, Phoenix, AZ, USA*, 2018, pp. 4–7.
- [72] S. Ioffe and C. Szegedy, “Batch normalization: Accelerating deep network training by reducing internal covariate shift,” in *International conference on machine learning*. pmlr, 2015, pp. 448–456.
- [73] A. L. Maas, A. Y. Hannun, A. Y. Ng et al., “Rectifier nonlinearities improve neural network acoustic models,” in *Proc. icml*, vol. 30, no. 1. Atlanta, Georgia, USA, 2013, p. 3.
- [74] F. Herrera, F. Charte, A. J. Rivera, M. J. Del Jesus, F. Herrera, F. Charte, A. J. Rivera, and M. J. del Jesus, *Multilabel classification*. Springer, 2016.
- [75] K. He, X. Zhang, S. Ren, and J. Sun, “Deep residual learning for image recognition,” in *Proceedings of the IEEE conference on computer vision and pattern recognition*, 2016, pp. 770–778.
- [76] V. Krishnamurthy and M. Levoy, “Fitting smooth surfaces to dense polygon meshes,” in *Proceedings of the 23rd annual conference on Computer graphics and interactive techniques*, 1996, pp. 313–324.
- [77] S. Hinterstoisser, V. Lepetit, S. Ilic, S. Holzer, G. Bradski, K. Konolige, and N. Navab, “Model based training, detection and pose estimation of texture-less 3d objects in heavily cluttered scenes,” in *Asian conference on computer vision*. Springer, 2012, pp. 548–562.
- [78] R. Kaskman, S. Zakharov, I. Shugurov, and S. Ilic, “Homebreweddb: Rgb-d dataset for 6d pose estimation of 3d objects,” in *Proceedings of the IEEE/CVF International Conference on Computer Vision Workshops*, 2019, pp. 0–0.
- [79] E. Rodola, A. Albarelli, F. Bergamasco, and A. Torsello, “A scale independent selection process for 3d object recognition in cluttered scenes,” *International journal of computer vision*, vol. 102, pp. 129–145, 2013.
- [80] F. Wang, Y. Zhuang, H. Gu, and H. Hu, “Octreenet: A novel sparse 3-d convolutional neural network for real-time 3-d outdoor scene analysis,” *IEEE Transactions on Automation Science and Engineering*, vol. 17, no. 2, pp. 735–747, 2019.
- [81] D. P. Kingma and J. Ba, “Adam: A method for stochastic optimization,” in *Proceedings of the 3rd International Conference on Learning Representations, ICLR*, 2015.
- [82] H. Yervilla-Herrera, J. I. Vasquez-Gomez, R. Murrieta-Cid, I. Becerra, and L. E. Sucar, “Optimal motion planning and stopping test for 3-d object reconstruction,” *Intelligent Service Robotics*, vol. 12, pp. 103–123, 2019.
- [83] H. Yervilla-Herrera, I. Becerra, R. Murrieta-Cid, L. E. Sucar, and E. F. Morales, “Bayesian probabilistic stopping test and asymptotic shortest time trajectories for object reconstruction with a mobile manipulator robot,” *Journal of Intelligent & Robotic Systems*, vol. 105, no. 4, p. 82, 2022.
- [84] M. Quigley, K. Conley, B. Gerkey, J. Faust, T. Foote, J. Leibs, R. Wheeler, A. Y. Ng et al., “Ros: an open-source robot operating system,” in *ICRA workshop on open source software*, vol. 3, no. 3.2. Kobe, Japan, 2009, p. 5.
- [85] A. Boulch and R. Marlet, “Poco: Point convolution for surface reconstruction,” in *Proceedings of the IEEE/CVF Conference on Computer Vision and Pattern Recognition*, 2022, pp. 6302–6314.
- [86] A. Nguyen and B. Le, “3d point cloud segmentation: A survey,” in *2013 6th IEEE conference on robotics, automation and mechatronics (RAM)*. IEEE, 2013, pp. 225–230.
- [87] T. Zaenker, J. Rückin, R. Menon, M. Popović, and M. Bennewitz, “Graph-based view motion planning for fruit detection,” *2023 IEEE/RSJ International Conference on Intelligent Robots and Systems (IROS)*, 2023.